RESEARCH ARTICLE

Early Tumor–Immune Microenvironmental Remodeling and Response to First-Line Fluoropyrimidine and Platinum Chemotherapy in Advanced Gastric Cancer

Ryul Kim[1], Minae An[2], Hyuk Lee[3], Arnav Mehta[4,5,6], You Jeong Heo[2], Kyoung-Mee Kim[7], Song-Yi Lee[1], Jeonghyeon Moon[8], Seung Tae Kim[1], Byung-Hoon Min[3], Tae Jun Kim[3], Sun Young Rha[9], Won Ki Kang[1], Woong-Yang Park[8,10], Samuel J. Klempner[5,11], and Jeeyun Lee[1,12]

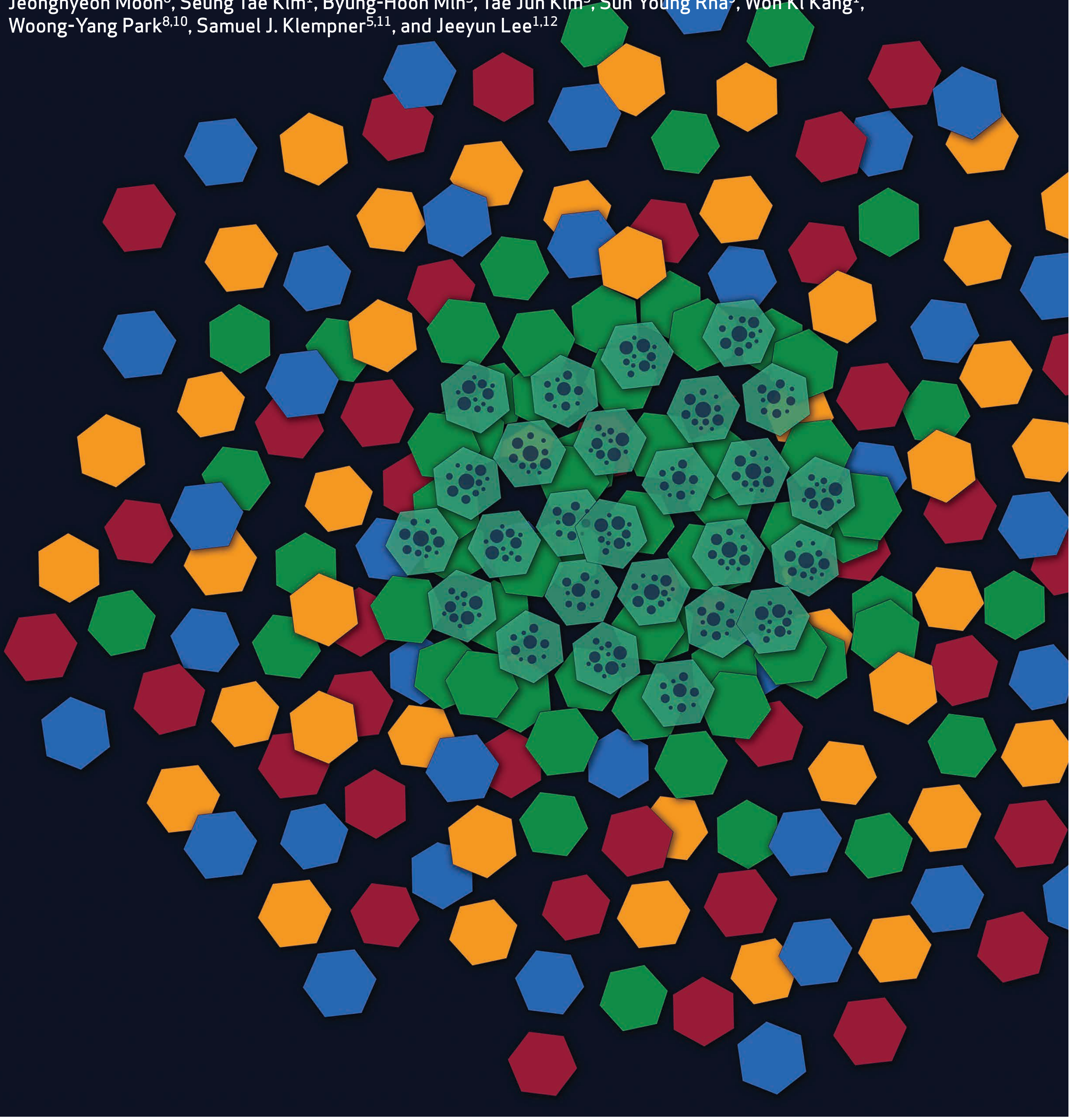

ABSTRACT Chemotherapy is ubiquitous in first-line treatment of advanced gastric cancer, yet responses are heterogeneous, and little is known about mediators of chemotherapy response. To move forward, an understanding of the effects of standard chemotherapy on the tumor–immune microenvironment (TME) is needed. Coupling whole-exome sequencing, bulk RNA and single-cell transcriptomics from paired pretreatment and on-treatment samples in treatment-naïve patients with HER2-positive and HER2-negative gastric cancer, we define features associated with response to platinum-based chemotherapy. Response was associated with on-treatment TME remodeling including natural killer (NK) cell recruitment, decreased tumor-associated macrophages, M1-macrophage repolarization, and increased effector T-cell infiltration. Among chemotherapy nonresponders, we observed low/absent PD-L1 expression or modulation, on-treatment increases in WNT signaling, B-cell infiltration, and LAG3-expressing T cells coupled to an exodus of dendritic cells. We did not observe significant genomic changes in early on-treatment sampling. We provide a map of on-treatment TME modulation with standard chemotherapy and nominate candidate future approaches.

SIGNIFICANCE: Using paired pretreatment and on-treatment samples during standard first-line chemotherapy, we identify chemotherapy-induced NK-cell infiltration, macrophage repolarization, and increased antigen presentation among responders. Increased LAG3 expression and decreased dendritic cell abundance were seen in nonresponders, emphasizing remodeling of the TME during chemotherapy response and resistance.

INTRODUCTION

Gastric cancer is the fifth most common malignancy and the third leading cause of cancer-related death worldwide (1, 2). Most patients present with locally advanced or metastatic disease, and median survival is 12 to 15 months (3–6).

Recently, several international phase III trials have validated the combination of anti–PD-1 agents with standard first-line 5-fluoropyrimidine and platinum chemotherapy in gastroesophageal cancers (7–11). Notably, the global phase III CheckMate-649 trial showed the efficacy of nivolumab in combination with chemotherapy as first-line treatment for advanced gastric cancer (AGC), leading to its accelerated approval by the FDA in April 2021 (9). Subsequently, interim analysis of the ongoing KEYNOTE-811 trial demonstrated the efficacy of first-line pembrolizumab in combination with trastuzumab and chemotherapy in locally advanced or metastatic HER2-positive AGC, leading to FDA approval in May 2021 (12). A recurring observation among phase III gastric and esophageal trials combining chemotherapy and immunotherapy has been differential activity based on PD-L1 expression (13). For example, in the CheckMate-649 trial, the HR for overall survival was 0.92 [95% confidence interval (CI), 0.70–1.23] and 0.94 (95% CI, 0.78–1.13) for PD-L1 combined positive score (CPS) <1 and <5, respectively, highlighting the lack of benefit in PD-L1^{lo} AGCs (9). The differential outcomes between patients with PD-L1^{hi} and PD-L1^{lo} tumors suggest the need for deeper understanding of the cellular and molecular mechanisms of response in gastroesophageal cancers.

---

[1]Division of Hematology-Oncology, Department of Medicine, Samsung Medical Center, Sungkyunkwan University School of Medicine, Seoul, Korea. [2]Samsung Advanced Institute of Health Science and Technology, Sungkyunkwan University School of Medicine, Seoul, Korea. [3]Department of Gastroenterology, Samsung Medical Center, Sungkyunkwan University School of Medicine, Seoul, Korea. [4]The Broad Institute of MIT and Harvard, Cambridge, Massachusetts. [5]Division of Hematology-Oncology, Department of Medicine, Massachusetts General Hospital, Boston, Massachusetts. [6]Dana-Farber Cancer Institute, Boston, Massachusetts. [7]Department of Pathology and Translational Genomics, Samsung Medical Center, Sungkyunkwan University School of Medicine, Seoul, Korea. [8]Geninus Inc., Seoul, Korea. [9]Department of Medical Oncology, Yonsei Cancer Center, Yonsei University College of Medicine, Seoul, Korea. [10]Samsung Genome Institute, Samsung Medical Center, Seoul, Korea. [11]Harvard Medical School, Boston, Massachusetts. [12]Department of Intelligent Precision Healthcare Convergence, Sungkyunkwan University, Suwon, Korea.

R. Kim, M. An, H. Lee, and A. Mehta contributed equally as co–first authors of this article.

Corresponding Authors: Samuel J. Klempner, Massachusetts General Hospital, 55 Fruit Street, Boston, MA 02114. Phone: 617-724-4000; Fax: 617-726-0452; E-mail: sklempner@partners.org; Woong-Yang Park, Department of Health Sciences and Technology, SAIHST, Samsung Medical Center Sungkyunkwan University, 81 Irwon-ro, Gangnam-gu, Seoul 06351, Korea. Phone: 82-2-2148-9810; Fax: 82-2-2148-9819; E-mail: woongyang.park@samsung.com; and Jeeyun Lee, Department of Intelligent Precision Healthcare Convergence, Sungkyunkwan University, Suwon, Korea. Phone: 82-2-3410-1779; Fax: 82-2-3410-1754; E-mail: jyunlee@skku.edu

Cancer Discov 2022;12:984–1001

doi: 10.1158/2159-8290.CD-21-0888

This open access article is distributed under the Creative Commons Attribution-NonCommercial-NoDerivatives 4.0 International (CC BY-NC-ND 4.0) license.

©2021 The Authors; Published by the American Association for Cancer Research

Cytotoxic chemotherapy plays a central role in AGC, including tumor debulking, leading to symptom palliation. The prevailing hypothesis for improvement in outcomes with the addition of immunotherapy to chemotherapy regimens is that cytotoxic chemotherapies may remodel the tumor–immune microenvironment (TME) and facilitate immune-mediated tumor killing, which can be potentiated with PD-1 blockade and reinvigoration of antitumor T-cell responses (14, 15). Platinum agents including oxaliplatin may upregulate PD-L1 expression on dendritic cells (DC) and enhance immune cell infiltration in murine colorectal models (16, 17). Preclinically, the antimetabolite 5-fluorouracil (5-FU) may facilitate antigen presentation by DCs while also exerting selective killing of myeloid-derived suppressor cells (MDSC; refs. 18, 19). Although 5-FU and oxaliplatin have preclinical evidence of the potential to induce favorable immunogenic conditions in the tumor microenvironment, we do not have direct evidence that this occurs in patients. A detailed understanding of the pretreatment and on-treatment TME during standard 5-FU/platinum alone in AGC remains a significant knowledge gap and barrier to better understanding our clinical data with PD-1 combinations.

To address these unmet needs, we sought to comprehensively characterize pre- and on-treatment biopsy tissues from patients with AGC undergoing first-line standard chemotherapy without PD-1 blockade. We performed whole-exome sequencing (WES), whole-transcriptome sequencing (WTS), single-cell RNA sequencing (scRNA-seq), and multiplexed immunofluorescence (mIF) to characterize the tumoral and immune compartments before and during 5-FU and platinum chemotherapy. We provide some of the first high-resolution data in AGC that demonstrate TME changes between patients who went on to be treatment responders or nonresponders to standard first-line chemotherapy. Our work may inform approaches to target the TME to expand the portion of patients benefiting from chemotherapy and the combination of chemotherapy and immunotherapy.

RESULTS

Patient Characteristics and Study Samples

The primary cohort consisted of 12 chemotherapy-naïve Korean patients with metastatic AGC, diagnosed between November 2018 and May 2019 at Samsung Medical Center (Seoul, Korea; Table 1). The median age was 56 (range, 33–75) years old. Five patients (41.7%) had HER2-positive AGC, and seven patients (58.3%) had PD-L1–positive tumors. There were no Epstein–Barr virus–positive or microsatellite instability–high patients. Five patients exhibited partial response (responder) to two cycles of first-line chemotherapy, whereas stable disease and progressive disease were observed in three and four patients, respectively (nonresponder; Fig. 1A and B). Patient EP12 was known to have progressed but was lost to follow-up and not considered evaluable. All patients underwent a pretreatment biopsy that was processed for WES and WTS, and five patients underwent on-treatment biopsies processed for WES and WTS. In addition, pretreatment and on-treatment scRNA-seq from fresh biopsies was performed on 11 and 7 patients, respectively (Fig. 1A). All tissue samples were taken from the primary tumor, and an attempt was made to biopsy the same area in all paired samples.

Table 1. Clinicopathologic features of study patients

Clinical characteristics	Values
Age, median (range)	55.5 (33–75) years
Sex, *n* (%)	
Male	8 (66.7%)
Female	4 (33.3%)
HER2, *n* (%)	
Positive	5 (41.7%)
Negative	7 (58.3%)
Primary tumor location, *n* (%)	
Cardia	1 (8.3%)
Body	8 (66.7%)
Antrum	3 (25.0%)
PD-L1 CPS, *n* (%)	
≥1	7 (58.3%)
0	5 (41.7%)
First-line treatment, *n* (%)	
XELOX	7 (58.3%)
XP + Trastuzumab	5 (41.7%)
Pathology, *n* (%)	
Moderately differentiated	5 (41.7%)
Poorly differentiated	5 (41.7%)
Signet ring cell	2 (16.6%)

Exonic Mutational Landscape of Study Samples

According to The Cancer Genome Atlas (TCGA) classifications, three patients had genomically stable (GS) tumors, whereas the remaining nine patients were chromosomally instable (20). We analyzed WES data of pretreatment and on-treatment samples (mean sequencing coverage of ~200× for tumor and matched blood samples) and found high-confidence somatic mutations, including 1,454 base substitutions and 49 indels in pretreatment samples and 534 base

Figure 1. Study overview and genomic landscape of enrolled patients. **A,** Experimental design. We obtained fresh tumor tissues from patients with AGC before and after two cycles of first-line chemotherapy. Response to the chemotherapy was performed using RECIST1.1 criterion (**B**). Patient EP12 was known to have progressed but was lost to follow-up and was not considered evaluable. The mutational landscape was analyzed in patients with HER2-positive AGC (**C**) and HER2-negative AGC (**D**). The negative sign in **C** and **D** indicates unavailable PD-L1 expression status, and hollow rectangle represents negative for PD-L1 expression. We summarized somatic mutations in selected canonical oncogenes and tumor-suppressor genes in AGC. Whole exome–derived tumor mutational burden and mutational signatures of somatic mutations in HER2-positive AGC (**E**) and HER2-negative AGC (**F**). The signature of exonic somatic SBSs was delineated by COSMIC signatures, which were represented by the following terms: age (SBS1 and SBS5), APOBEC (apolipoprotein B mRNA editing enzyme; SBS2 and SBS13), UV (ultraviolet; SBS7a, SBS7b, SBS7c, and SBS7d), TMZ (temozolomide, SBS11), smoking (SBS4), immunoglobulin gene hypermutation (SBS9), HRD (homologous recombination deficiency; SBS3), MMRD (mismatch repair deficiency; SBS6, SBS15, SBS20, and SBS26), NERD (nucleotide excision repair deficiency; SBS8), DPD (DNA proofreading deficiency; SBS10a and SBS10b), BERD (base excision repair deficiency; SBS18), chemotherapy (SBS25), and platinum treatment (SBS31, SBS35). The size of the circles reflecting the mutational signatures corresponds to the proportion of the signature in the sample. BoR, best of response; CIN, chromosomal instability; GC, gastric cancer; PD, progressive disease; SD, stable disease; PR, partial response.

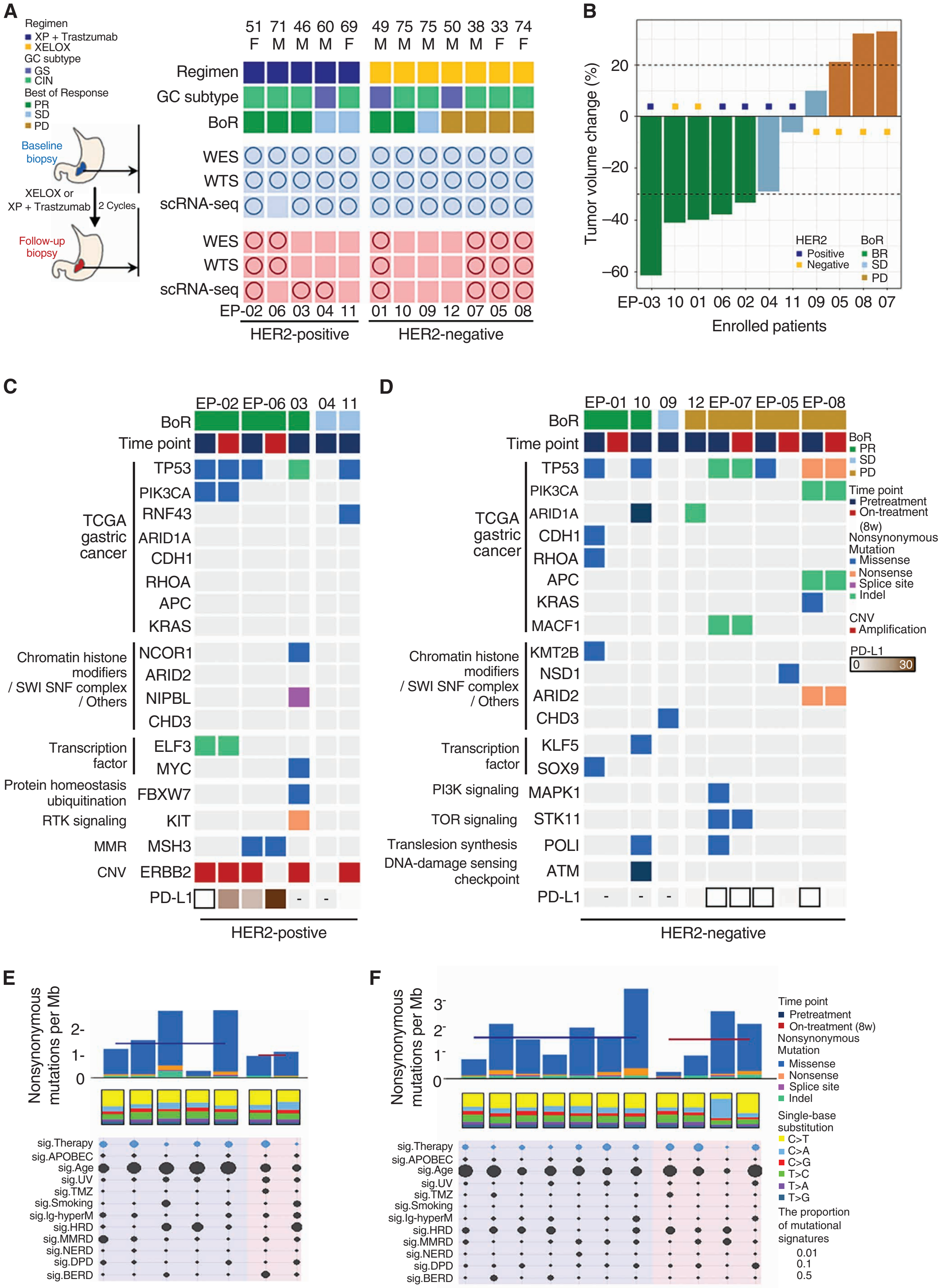
A
Regimen
XP + Trastzumab
XELOX
GC subtype
GS
CIN
Best of Response
PR
SD
PD
Baseline biopsy
XELOX or XP + Trastzumab
2 Cycles
Follow-up biopsy
51 71 46 60 69 49 75 75 50 38 33 74
F M M M F M M M M M F F
Regimen
GC subtype
BoR
WES
WTS
scRNA-seq
WES
WTS
scRNA-seq
EP-02 06 03 04 11 01 10 09 12 07 05 08
HER2-positive
HER2-negative
B
Tumor volume change (%)
20
0
−20
−40
−60
HER2
Positive
Negative
BoR
BR
SD
PD
EP-03 10 01 06 02 04 11 09 05 08 07
Enrolled patients
C
EP-02 EP-06 03 04 11
BoR
Time point
TCGA gastric cancer
TP53
PIK3CA
RNF43
ARID1A
CDH1
RHOA
APC
KRAS
Chromatin histone modifiers / SWI SNF complex / Others
NCOR1
ARID2
NIPBL
CHD3
Transcription factor
ELF3
MYC
Protein homeostasis ubiquitination
FBXW7
RTK signaling
KIT
MMR
MSH3
CNV
ERBB2
PD-L1
-
-
HER2-postive
D
EP-01 10 09 12 EP-07 EP-05 EP-08
BoR
Time point
TCGA gastric cancer
TP53
PIK3CA
ARID1A
CDH1
RHOA
APC
KRAS
MACF1
Chromatin histone modifiers / SWI SNF complex / Others
KMT2B
NSD1
ARID2
CHD3
Transcription factor
KLF5
SOX9
PI3K signaling
MAPK1
TOR signaling
STK11
Translesion synthesis
POLI
DNA-damage sensing checkpoint
ATM
PD-L1
-
-
-
HER2-negative
BoR
PR
SD
PD
Time point
Pretreatment
On-treatment (8w)
Nonsynonymous Mutation
Missense
Nonsense
Splice site
Indel
CNV
Amplification
PD-L1
0
30
E
Nonsynonymous mutations per Mb
2
1
0
sig.Therapy
sig.APOBEC
sig.Age
sig.UV
sig.TMZ
sig.Smoking
sig.Ig-hyperM
sig.HRD
sig.MMRD
sig.NERD
sig.DPD
sig.BERD
F
Nonsynonymous mutations per Mb
3
2
1
0
sig.Therapy
sig.APOBEC
sig.Age
sig.UV
sig.TMZ
sig.Smoking
sig.Ig-hyperM
sig.HRD
sig.MMRD
sig.NERD
sig.DPD
sig.BERD
Time point
Pretreatment
On-treatment (8w)
Nonsynonymous Mutation
Missense
Nonsense
Splice site
Indel
Single-base substitution
C>T
C>A
C>G
T>C
T>A
T>G
The proportion of mutational signatures
0.01
0.1
0.5

substitutions and 18 indels in on-treatment samples. Consistent with prior reports, we observed mutations in genes enriched in the TCGA gastric cancer cohort including chromatin histone modifiers and transcription factors (Fig. 1C and D). Mutations in *TP53*, *PIK3CA*, *APC*, *ELF3*, *MACF1*, *ARID2*, and *MSH3* were shared between pretreatment and on-treatment samples, suggesting clonal mutations occurred in most recent common ancestors of the two samples and preservation of tumor clones with these mutations during treatment. To characterize the mutational processes that generate point mutations in AGC, we analyzed mutational signatures for the 18 WES from AGC tissue (12 pretreatment and 6 on-treatment samples) on the COSMIC catalog (ref. 21; Fig. 1E and F). Most single-nucleotide substitutions (SBS) were C:G>T:A transition. The mutational spectrums suggest that previously defined mutational signatures of endogenous processes, associated with 5-methylcytosine deamination and correlated with age, were responsible for the somatic single-nucleotide variants (SNV) of AGC. Overall, there were limited early genomic changes observed with two cycles of platinum-based chemotherapy, suggesting that early mutational changes were not the predominant mediator of TME changes discussed below.

Chemotherapy Reshapes the Gastric Cancer TME toward Immune-Responsive Features

After observing limited early changes in the tumor mutational landscape or mutational signature composition on treatment, we focused our attention on the immune components of the TME. We integrated RNA-seq data from 12 pretreatment and 6 on-treatment samples to characterize the immune microenvironment of AGC. We then sought to apply recent pan-cancer TME signatures to examine the ability of chemotherapy to affect signatures associated with immunotherapy response (22). By integrating the transcriptomic data, we classified each tumor sample into four previously defined distinct microenvironment subtypes (immune-depleted, fibrotic, immune-enriched, and immune-enriched/fibrotic) using the molecular functional portrait (Fig. 2A). In the primary cohort, we did not observe clear baseline differences in TME composition between responder and nonresponder patients (Fig. 2A). To screen specific gene set enrichment in on-treatment over pretreatment samples, we performed gene set variation analysis (GSVA; ref. 23; Fig. 2B). Genes in several canonical pathways showed distinctive pattern of enrichments between pre- and on-treatment samples. Notably, genes related to M2-oriented macrophages (anti-inflammatory, immunosuppressive) were significantly repressed across the cohort in posttreatment samples (P = 0.009), indicating increased M1/M2 repolarization during conventional chemotherapy (24). Significant activation of the PD-1 pathway was seen in on-treatment samples (P = 0.033), suggesting capecitabine plus oxaliplatin (XELOX) or capecitabine plus cisplatin/trastuzumab (XPT) chemotherapy is reshaping the TME of AGC, especially in responders. Notably, on-treatment increases in the PD-1 pathway and inflammasome were more common among responders. Conversely, on-treatment WNT-pathway increases were enriched among nonresponders and may function to limit T-cell infiltration (25).

Chemotherapy Modulates T-cell Populations within the TME

To describe the changes in the TME of AGC by fluoropyrimidine plus platinum agents, we examined single-cell gene expression profiles of pretreatment (n = 11) and on-treatment (n = 7) biopsies. After filtering low-quality cells and applying batch correction (using Harmony), we collected a total of 18,911 cells (10,651 cells from pretreatment samples and 8,260 cells from on-treatment samples; ref. 26). We next performed unsupervised clustering and identified seven major cell types using tissue type–specific canonical marker genes previously defined in the literature (27): epithelial cells (n = 3,056), stromal cells (n = 3,750), T cells (n = 7,145), natural killer (NK) cells (n = 624), myeloid cells (n = 1,902), B cells (n = 1,877), and platelets and undefined cells (n = 557; Fig. 2C; Supplementary Fig. S1A and S1B). The T-cell proportion showed a tendency to increase in on-treatment samples, especially in HER2-negative AGC (Fig. 2D, top). Responders had a higher proportion of effector CD8 cells in on-treatment samples (median, 46.1%; range, 45.3%–48.0%) compared with pretreatment samples (median, 39.5%; range, 35.0%–54.7%; Fig. 2D, right middle). A decrease in T regulatory cells (Treg) on treatment was observed only in responders. On the other hand, in nonresponders, the proportion of exhausted T cells increased in on-treatment samples (median, 14.0%; range, 8.7%–33.8%) compared with pretreatment samples (median, 10.5%; range, 5.0%–42.1%; Fig. 2D, right middle). Compared with responders, nonresponders had a higher proportion of tumor-associated macrophages (TAM) in pretreatment samples (median, 79.1%; range, 37.0%–97.7%), and the proportion was increased in on-treatment samples (median, 86.7%; range, 75.0%–92.3%; Fig. 2D).

Chemotherapy Activates Innate Immune Pathways in Tumor Cells

To gain insight into mechanisms underlying the increased abundance of T cells in the TME while on chemotherapy, we

Figure 2. 5-FU and platinum remodel the TME in AGC. **A,** Immune score of pretreatment and on-treatment samples from patients with HER2-positive and HER2-negative AGC (left), and responders and nonresponders (right). Heat map of GSVA scores of representative pathways across pretreatment (n = 12) and on-treatment (n = 6) samples (**B**). We performed the Wilcoxon signed-rank test to assess the differences in G-scores between pretreatment and posttreatment samples, between HER2-positive and HER2-negative pretreatment samples, and between HER2-positive and HER2-negative posttreatment samples. The P values are illustrated on right side of the heat map using bar plots. EMT, epithelial–mesenchymal transition. **C,** Uniform manifold approximation and projection (UMAP) embedding of 18,911 cells (10,651 cells from pretreatment samples and 8,260 cells from posttreatment samples). Multiple clusters represent various cell types in the TME of AGC. **D,** Relative proportion of cell subtypes of pretreatment and on-treatment samples from patients with HER2-positive and HER2-negative AGC (left), and responders and nonresponders (right). Global cell types, T-cell, and myeloid subpopulations are illustrated in top, middle, and bottom plots, respectively. **E,** The RNA expression of genes involved in innate immune response and immunogenic cell death: *ANXA1*, *HMGB1*, *CGAS*, and *STING*. We estimated the expression using scRNA-seq of pretreatment and posttreatment samples from patients with HER2-positive and HER2-negative AGC. The box plots describe the median and interquartile range of the expression. The P values were estimated by the Wilcoxon signed-rank test.

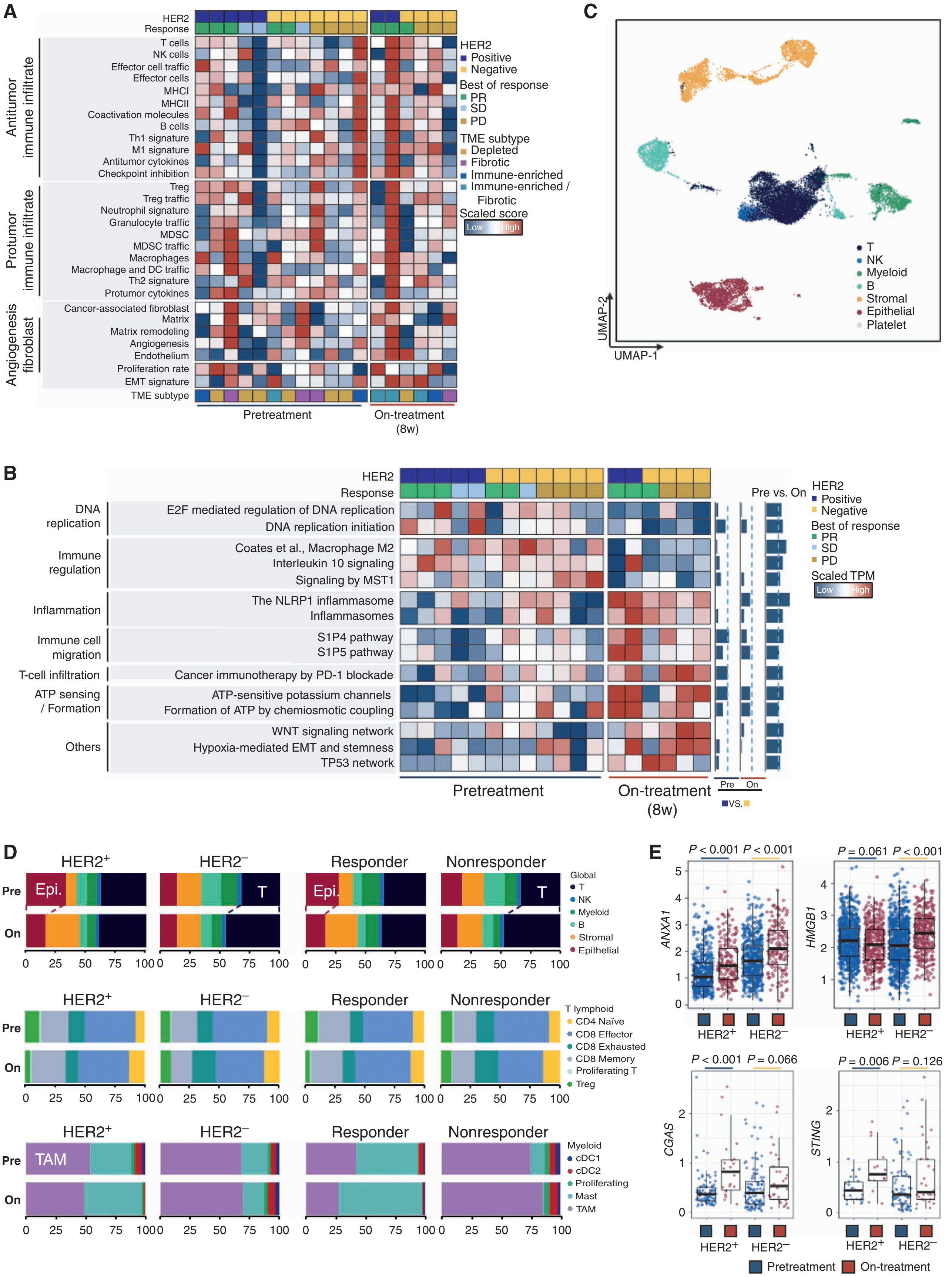
A
HER2
Response
Antitumor immune infiltrate
T cells
NK cells
Effector cell traffic
Effector cells
MHCI
MHCII
Coactivation molecules
B cells
Th1 signature
M1 signature
Antitumor cytokines
Checkpoint inhibition
Protumor immune infiltrate
Treg
Treg traffic
Neutrophil signature
Granulocyte traffic
MDSC
MDSC traffic
Macrophages
Macrophage and DC traffic
Th2 signature
Protumor cytokines
Angiogenesis fibroblast
Cancer-associated fibroblast
Matrix
Matrix remodeling
Angiogenesis
Endothelium
Proliferation rate
EMT signature
TME subtype
Pretreatment
On-treatment (8w)
HER2
Positive
Negative
Best of response
PR
SD
PD
TME subtype
Depleted
Fibrotic
Immune-enriched
Immune-enriched / Fibrotic
Scaled score
Low
High
C
T
NK
Myeloid
B
Stromal
Epithelial
Platelet
UMAP-2
UMAP-1
B
HER2
Response
DNA replication
E2F mediated regulation of DNA replication
DNA replication initiation
Immune regulation
Coates et al., Macrophage M2
Interleukin 10 signaling
Signaling by MST1
Inflammation
The NLRP1 inflammasome
Inflammasomes
Immune cell migration
S1P4 pathway
S1P5 pathway
T-cell infiltration
Cancer immunotherapy by PD-1 blockade
ATP sensing / Formation
ATP-sensitive potassium channels
Formation of ATP by chemiosmotic coupling
Others
WNT signaling network
Hypoxia-mediated EMT and stemness
TP53 network
Pretreatment
On-treatment (8w)
Pre vs. On
Pre
On
VS.
HER2
Positive
Negative
Best of response
PR
SD
PD
Scaled TPM
Low
High
D
HER2+
HER2−
Responder
Nonresponder
Pre
On
Epi.
T
Epi.
T
0 25 50 75 100
Global
T
NK
Myeloid
B
Stromal
Epithelial
T lymphoid
CD4 Naïve
CD8 Effector
CD8 Exhausted
CD8 Memory
Proliferating T
Treg
TAM
Myeloid
cDC1
cDC2
Proliferating
Mast
TAM
E
P < 0.001 P < 0.001
ANXA1
0 1 2 3 4 5
P = 0.061 P < 0.001
HMGB1
1 2 3 4
P < 0.001 P = 0.066
CGAS
0 1 2
P = 0.006 P = 0.126
STING
0 1 2
HER2+ HER2−
Pretreatment
On-treatment

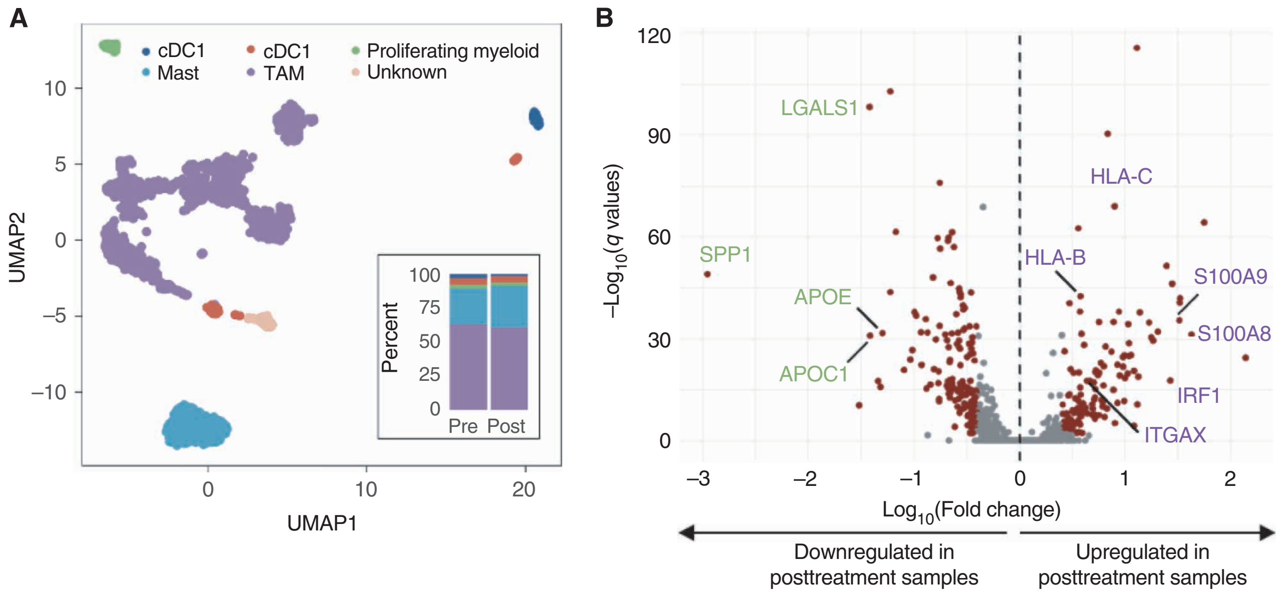

Figure 3. Transcriptional reprogramming of TAMs during first-line chemotherapy. **A,** UMAP embedding 1,902 myeloid cell population of scRNA-seq data. Multiple clusters represent various subtypes of myeloid cells in the TME of AGC. Bar plots demonstrating relative proportions of myeloid subtypes in pretreatment and posttreatment AGC samples (plot **A** inset). **B,** A volcano plot showing differentially expressed genes in scRNA-seq data between pretreatment and on-treatment samples. Genes marked in green and purple are related to M2 and M1 macrophage states, respectively. (*continued on following page*)

investigated immune signaling pathways within the epithelial cell population (2,011 cells from pretreatment samples and 1,045 cells from on-treatment samples; Fig. 2E). Notably, the expression of representative genes in the damage-associated molecular patterns family, including Annexin A1 (*ANXA1*) and high mobility group box 1 (*HMGB1*; ref. 28), increased after chemotherapy in HER2-positive ($P = 0.001$) and HER2-negative ($P < 0.001$) patients with AGC. In addition, genes involved in innate immune signaling, such as cyclic GMP-AMP synthase (cGAS) and STING (transmembrane protein 173, also known as TMEM173; ref. 29), showed increased expression in HER2-positive on-treatment samples, consistent with prior data that HER2 inhibition induces STING pathway activation (30). Collectively, these data suggest conventional cytotoxic chemotherapy may promote antitumor inflammation within the TME of AGC by reorganizing the T-cell compartment and inducing innate signaling pathways in tumor cells in a subset of patients.

Chemotherapy Reprograms TAMs

We next hypothesized that antigen-presenting cells may play an important role in reorganizing the TME and recruiting T cells in the setting of chemotherapy. We therefore clustered 1,902 myeloid cells (1,104 cells from pretreatment samples and 798 cells from posttreatment samples) into 5 major subtypes and focused on TAMs (n = 1,425; Fig. 3A; Supplementary Fig. S2A). We identified 1,003 differentially expressed genes between pretreatment and on-treatment samples. Among those, proinflammatory genes, such as *S100A8*, *S100A9*, *IRF1*, and *ITGAX* (31–33), and MHC class I antigen-presentation genes, such as HLA-B and HLA-C, were significantly upregulated in on-treatment samples, whereas anti-inflammatory molecules such as *SPP1*, *LGALS1*, *APOE*, and *APOC1* (34–36) were downregulated while on chemotherapy (Fig. 3B). Next, to identify enriched pathways in scRNA-seq data, we calculated the module scores of canonical pathways. Concordant with the finding in GSVA analysis of WTS data (Fig. 2B), the expression of genes related to M2 (anti-inflammatory) macrophages decreased in on-treatment samples, especially in HER2-negative AGC samples ($P < 0.001$). On the other hand, genes associated with myeloid differentiation, antigen processing and presentation, and peptide loading on MHC1 molecule showed higher expression in on-treatment compared with pretreatment samples, consistent with chemotherapy-induced macrophage modulation (Fig. 3C).

To better understand the reorganization of macrophage phenotypes in the setting of chemotherapy, we reconstructed the differentiation trajectory of TAMs using the Slingshot toolkit (ref. 37; Fig. 3D). We set a cluster expressing monocyte-like macrophage markers (*CD14*, *FCN1*) as a start point and inferred the end point from pseudotime ordering. Interestingly, we observed two distinct trajectories, one of which stretched to genes specific to M2 macrophages, whereas the other stretched to M1 macrophage–related genes (Supplementary Fig. S2B). In pretreatment samples, the proportion of M2 macrophage (91.9%) was much higher than M1 macrophage (8.1%). However, subpopulations of TAMs in on-treatment samples skewed to M1 macrophage with a proportion of 35.8%. Taken together, these data indicate that conventional chemotherapy leads to increased M1/M2 polarization. To corroborate these observations, we examined paired biopsy samples from a responding patient (EP-02). Consistent with scRNA-seq data, we observed

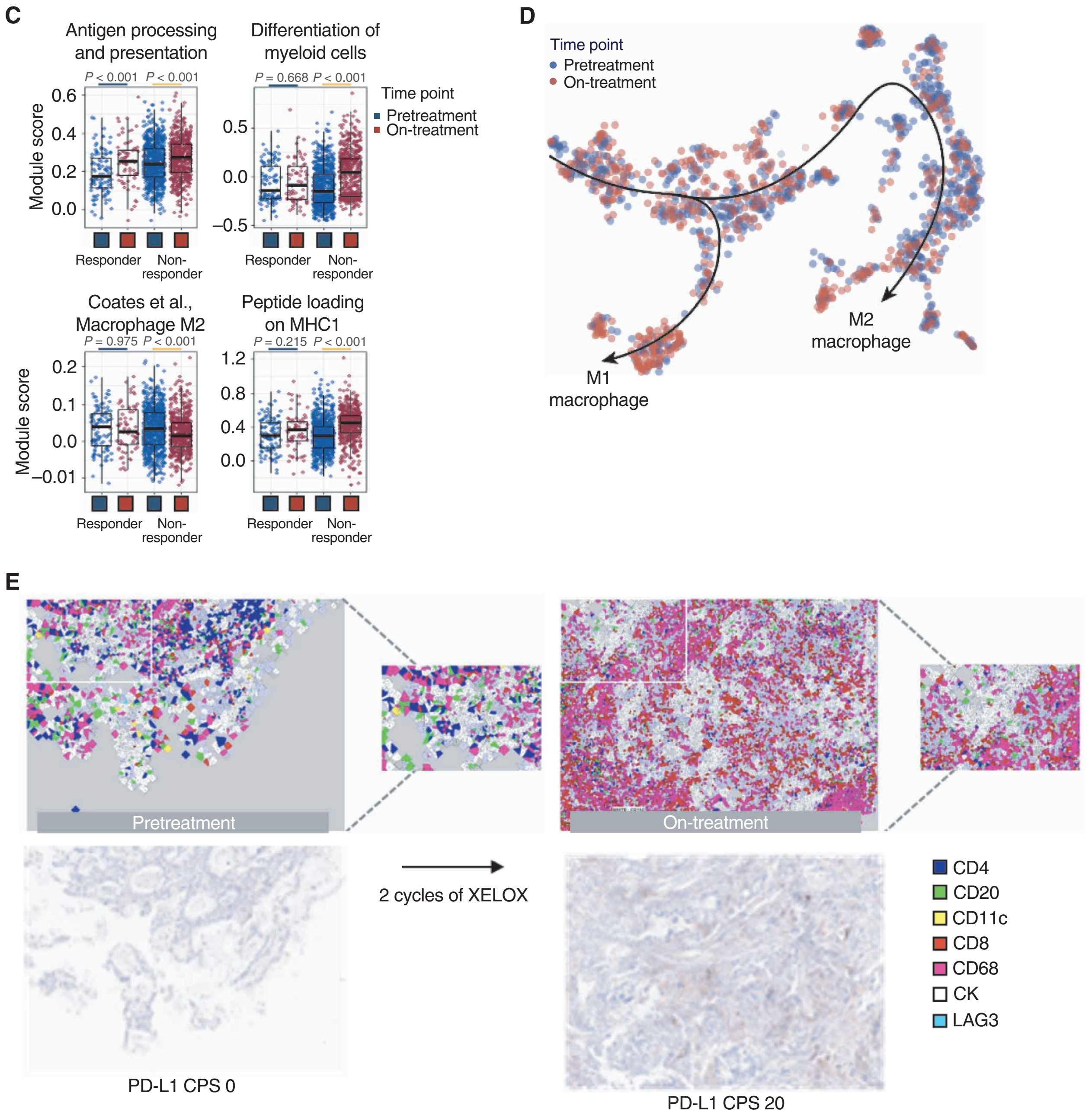

Figure 3. ***(Continued)*** **C,** Differentially enriched pathways in macrophages between pretreatment and on-treatment samples from responder and nonresponder patients with AGC. Module scores were estimated using an algorithm embedded in Seurat package. Box plots describe the median and interquartile range of the expression. Significance of differences was estimated by the Wilcoxon signed-rank test. **D,** Pseudotime trajectories of macrophages demonstrating different developmental trajectory in pretreatment and on-treatment samples. We used the Slingshot algorithm to reconstruct the trajectories. Each dot represents a macrophage in pretreatment (blue) and posttreatment (red) samples. **E,** mIF images characterizing the TME of AGC before and during first-line chemotherapy in a representative case (EP-02) who showed PD-L1 upregulation and response to chemotherapy.

a significant increase in CD8$^+$ lymphocyte infiltration (26,259,051 cells) from baseline (1,825,166 cells) and a considerable increase in CD68$^+$ macrophages from 3,646,753 cells to 46,421,747 cells during chemotherapy (Fig. 3E). However, CD68 cells cannot fully distinguish macrophage subtypes. Interestingly, this patient was PD-L1–negative (CPS = 0) at baseline but PD-L1–positive (CPS = 20) after two cycles of XELOX chemotherapy.

Independent External Validation of Early TME Remodeling by First-Line Chemotherapy

To validate findings in our primary cohort, we investigated the pretreatment and on-treatment tumor samples of a subset of 17 consecutively enrolled patients with AGC from an ongoing clinical trial (NCT04249739). This is a phase II trial of first-line chemotherapy [XELOX or capecitabine plus cisplatin (XP) + trastuzumab] plus pembrolizumab with preplanned baseline and follow-up biopsy after one cycle of chemotherapy prior to the addition of pembrolizumab. In this study, a total of 17 consecutive patients were included for this analysis, including 3 patients with HER2-positive AGC (Supplementary Table S1). On-treatment samples were collected after one cycle of 5-FU and platinum chemotherapy (oral capecitabine and oxaliplatin for HER2-negative AGC; trastuzumab plus oral capecitabine and cisplatin for HER2-positive AGC). We obtained pretreatment primary tumor and matched on-treatment tumor samples from the primary gastric tumor and performed WTS. Cell type deconvolution using the CibersortX algorithm revealed an increase in effector cell populations in the on-treatment TME (refs. 38, 39; Supplementary Fig. S3). Furthermore, the GSVA algorithm showed significantly repressed M2-oriented macrophages and activated PD-1 signaling in on-treatment samples, validating our previous scRNA-seq results (Fig. 4A). Interestingly, we observed additional on-treatment enrichment of pathways involved in T-cell receptor signaling, costimulation, and effector cells consistent with our primary cohort.

We again classified each tumor sample into four previously defined distinct TME subtypes using the molecular functional portrait (ref. 22; Fig. 4B). In a majority of patients, we observed a dynamic change after one cycle of chemotherapy. Specifically, 7 (50.0%) out of 14 samples with immune-depleted or fibrotic pretreatment TME became immune-favorable during treatment (Fig. 4C). Interestingly, the pretreatment and on-treatment TME was more inflamed in HER2-positive than HER2-negative AGC, an observation that could partly underlie the high biological activity of PD-1 in combination with trastuzumab and hint at the immunomodulatory role for trastuzumab (ref. 40; Fig. 4D). After one cycle of the study treatment, expression signatures involved in effector cells (including T cells and Th1 cells), checkpoint inhibition, and MHC-II expression were significantly higher in both HER2-positive and HER2-negative AGC (Fig. 4E). Collectively, these results indicate early TME remodeling during anticancer treatment, corroborating and augmenting our previous results.

Early Increase in LAG3 Expression on T Cells Correlates with Lack of Benefit from First-Line Chemotherapy

Given the clear immune remodeling effects of chemotherapy, we next hypothesized that inability to effectively modulate the T-cell composition, specifically exhausted T-cell populations, may play a role in chemotherapy nonresponse. We subclustered a total of 7,145 T cells (3,693 cells from pretreatment samples and 3,452 cells from on-treatment samples) into six subtypes: Treg (*n* = 684), naïve CD4 (*n* = 863), proliferating T cells (*n* = 51), memory CD8 (*n* = 1,475), effector CD8 (*n* = 3,031), and exhausted CD8 (*n* = 1,041; Fig. 5A; Supplementary Fig. S4A). Exhausted CD8 cells were further subclassified to four stages according to established developmental groupings (Supplementary Fig. S4B; ref. 41). To understand shared features among nonresponders, we focused on EP-05, EP-07, and EP-08, who had *de novo* resistance to standard XELOX chemotherapy (Fig. 1A and B). We found that two patients had *MET* amplification in their primary gastric tumor, and all three patients were PD-L1 negative (CPS = 0) at baseline and failed to upregulate PD-L1 expression on chemotherapy. Interestingly, *TIGIT* expression was enriched in T cells of patients with *MET* amplification (Fig. 5B). Overall, *MET*-amplified patients had a higher proportion of terminally differentiated T cells compared with patients with wild-type *MET* (Fig. 5B).

To understand the spatial distribution of exhausted T cells, we focused on paired samples from a patient (EP-07) with *MET*-amplified AGC that had progressed rapidly during two cycles of XELOX chemotherapy (Fig. 5C). mIF with CODEX showed abundant CD11c$^+$ DCs (*n* = 857, 12.2%) and CD8$^+$ lymphocytes (*n* = 1545, 22.1%) around tumor at baseline; however, after two cycles of chemotherapy, the TME was infiltrated mostly with macrophages and tumor cells, CD20$^+$ B cells (*n* = 779, 8.6%), and near absence of DCs (*n* = 36; 0.4%; Fig. 5D). Another patient with progressive disease (EP-08) had a higher proportion of LAG3$^+$ (*n* = 35, 0.3%) and CD20$^+$ (*n* = 292, 2.5%) cells in on-treatment than in pretreatment tumor (LAG3$^+$ cells, *n* = 3, 0.04%; CD20$^+$ cells, *n* = 80, 1.09%; Fig. 5E). We observed a similar phenomenon in two other patients with primary progression (EP-05 and EP-07) as assessed by LAG3 protein expression in mIF as well as *LAG3* mRNA expression in scRNA-seq (Fig. 5F).

Although limited by small patient numbers, nonresponders to XELOX chemotherapy, all of whom were PD-L1 negative (Fig. 1D), failed to favorably remodel their TME and exhibited minimal change in T-cell infiltration but rather an increase in LAG3 expression and B-cell infiltration. Conversely, a trend toward these unfavorable TME features was not observed among responders to XELOX or XP/trastuzumab. Taken together, our overall data suggest a putative working model to correlate chemotherapy response with TME remodeling, which may provide a rationale for combination of chemotherapy and anti–PD-1 therapy (Fig. 6).

DISCUSSION

The complex interactions between tumor and immune/stromal cells play out in the TME and dictate clinical outcomes, including among patients with AGC (42–44). To optimally understand how to therapeutically target the gastric cancer TME, we need to first understand the effects of our current standard chemotherapy backbones which nearly all patients receive and which play a central role in treatment. In this work, conducted prior to FDA approval of combination

Figure 4. Independent validation of TME remodeling during 5-FU/platinum chemotherapy. **A,** Heat map of GSVA scores of representative pathways across pretreatment and on-treatment samples. **B,** Heat map demonstrating changes in relative TME composition, including changes in TME subtype signatures. The negative sign indicates unavailable PD-L1 expression status. **C,** Sankey plot demonstrating a dynamic change of TME subtype between pretreatment and posttreatment samples. **D** and **E,** Activity of selected molecular functional portraits (**D**) in pretreatment TME of HER2-positive (*n* = 3) and HER2-negative (*n* = 14) tumors, and (**E**) in on-treatment compared with pretreatment samples. Th1, T helper 1 cell; Th2, T helper 2 cell; TCR, T-cell receptor; EMT, epithelial–mesenchymal transition; PR, partial response; SD, stable disease; PD, progressive disease.

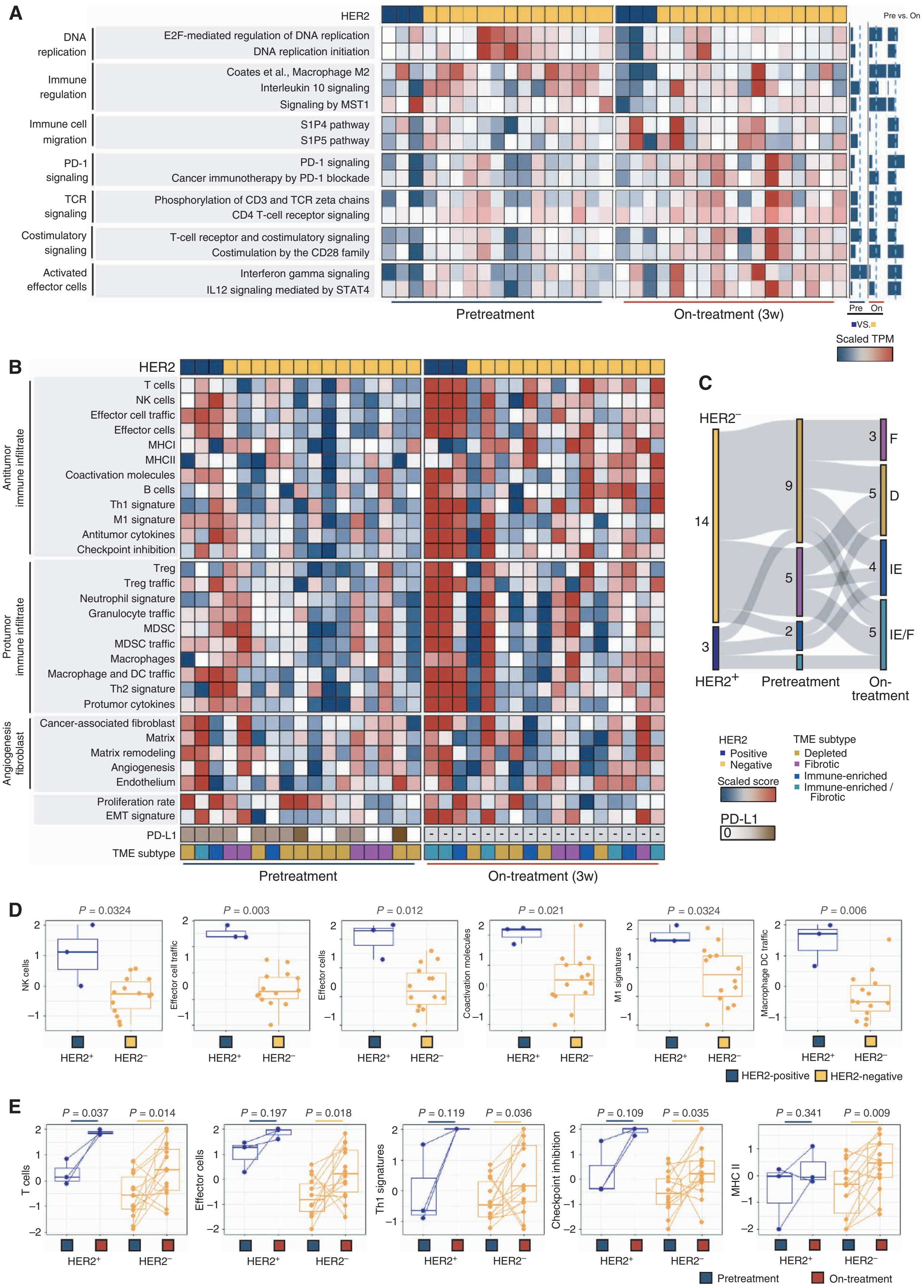
A
HER2
Pre vs. On
DNA replication
E2F-mediated regulation of DNA replication
DNA replication initiation
Immune regulation
Coates et al., Macrophage M2
Interleukin 10 signaling
Signaling by MST1
Immune cell migration
S1P4 pathway
S1P5 pathway
PD-1 signaling
PD-1 signaling
Cancer immunotherapy by PD-1 blockade
TCR signaling
Phosphorylation of CD3 and TCR zeta chains
CD4 T-cell receptor signaling
Costimulatory signaling
T-cell receptor and costimulatory signaling
Costimulation by the CD28 family
Activated effector cells
Interferon gamma signaling
IL12 signaling mediated by STAT4
Pretreatment
On-treatment (3w)
Pre On
■vs.■
Scaled TPM
B
HER2
Antitumor immune infiltrate
T cells
NK cells
Effector cell traffic
Effector cells
MHCI
MHCII
Coactivation molecules
B cells
Th1 signature
M1 signature
Antitumor cytokines
Checkpoint inhibition
Protumor immune infiltrate
Treg
Treg traffic
Neutrophil signature
Granulocyte traffic
MDSC
MDSC traffic
Macrophages
Macrophage and DC traffic
Th2 signature
Protumor cytokines
Angiogenesis fibroblast
Cancer-associated fibroblast
Matrix
Matrix remodeling
Angiogenesis
Endothelium
Proliferation rate
EMT signature
PD-L1
TME subtype
Pretreatment
On-treatment (3w)
C
HER2−
14
3
HER2+
9
5
2
Pretreatment
3 F
5 D
4 IE
5 IE/F
On-treatment
HER2
■ Positive
■ Negative
Scaled score
TME subtype
■ Depleted
■ Fibrotic
■ Immune-enriched
■ Immune-enriched / Fibrotic
PD-L1
0
D
P = 0.0324
NK cells
P = 0.003
Effector cell traffic
P = 0.012
Effector cells
P = 0.021
Coactivation molecules
P = 0.0324
M1 signatures
P = 0.006
Macrophage DC traffic
2
1
0
−1
HER2+
HER2−
■ HER2-positive ■ HER2-negative
E
P = 0.037
P = 0.014
T cells
P = 0.197
P = 0.018
Effector cells
P = 0.119
P = 0.036
Th1 signatures
P = 0.109
P = 0.035
Checkpoint inhibition
P = 0.341
P = 0.009
MHC II
2
1
0
−1
−2
HER2+
HER2−
■ Pretreatment ■ On-treatment

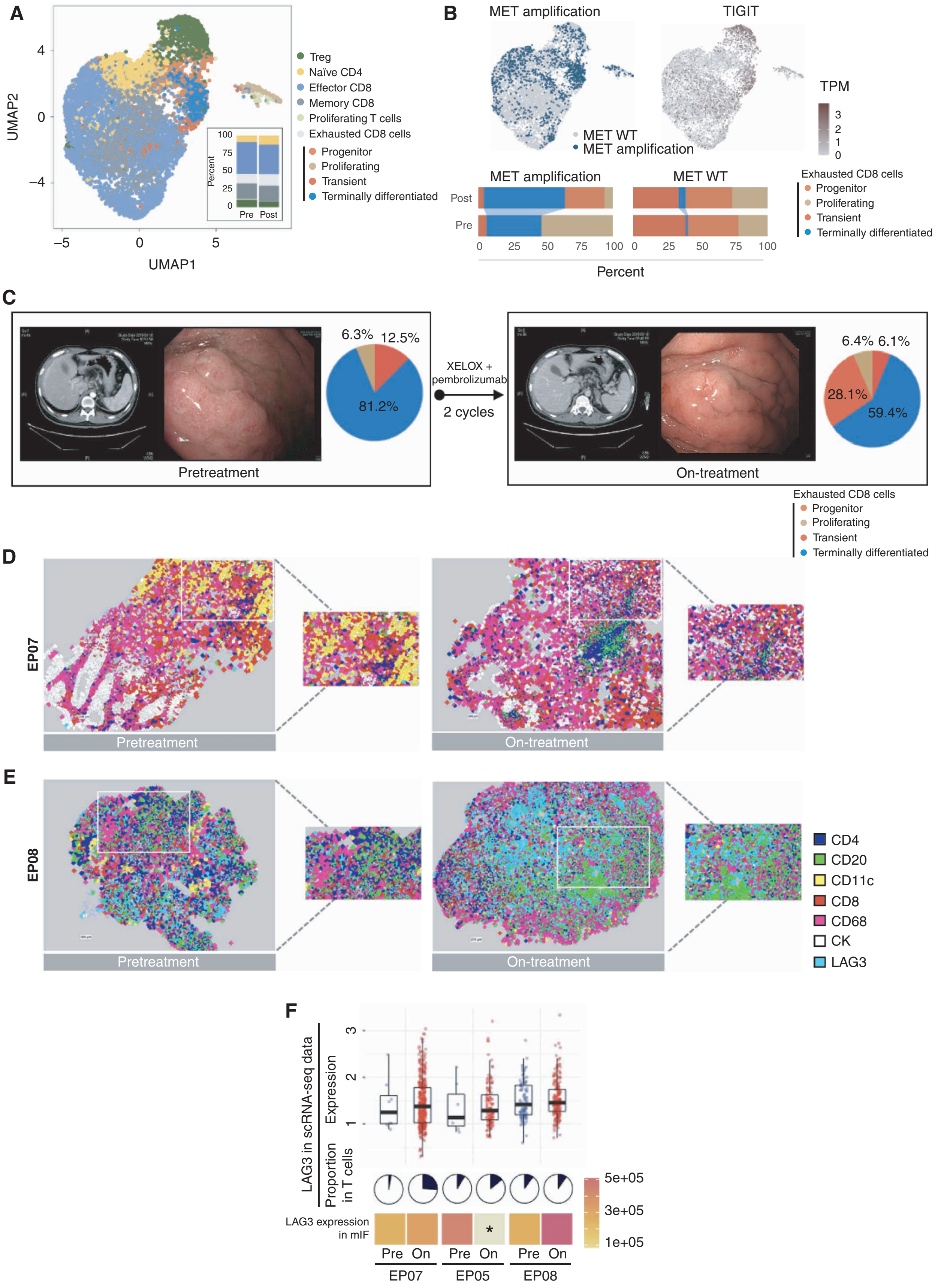
A
UMAP2
UMAP1
4
0
−4
−5
0
5
Percent
100
75
50
25
0
Pre
Post
Treg
Naïve CD4
Effector CD8
Memory CD8
Proliferating T cells
Exhausted CD8 cells
Progenitor
Proliferating
Transient
Terminally differentiated
B
MET amplification
TIGIT
MET WT
MET amplification
TPM
3
2
1
0
MET amplification
MET WT
Post
Pre
0
25
50
75
100
Percent
Exhausted CD8 cells
Progenitor
Proliferating
Transient
Terminally differentiated
C
6.3%
12.5%
81.2%
Pretreatment
XELOX +
pembrolizumab
2 cycles
6.4%
6.1%
28.1%
59.4%
On-treatment
Exhausted CD8 cells
Progenitor
Proliferating
Transient
Terminally differentiated
D
EP07
Pretreatment
On-treatment
E
EP08
Pretreatment
On-treatment
CD4
CD20
CD11c
CD8
CD68
CK
LAG3
F
LAG3 in scRNA-seq data
Expression
Proportion in T cells
1
2
3
LAG3 expression in mIF
*
5e+05
3e+05
1e+05
Pre
On
Pre
On
Pre
On
EP07
EP05
EP08

chemotherapy/immunotherapy, we coupled WTS and scRNA-seq from paired pretreatment and on-treatment samples in a cohort of Asian patients with AGC receiving standard 5-FU/platinum therapies with or without trastuzumab depending on standard HER2 testing.

Though we acknowledge the limitations of the small sample size, several clinically relevant themes emerge from our data, which represent the initial and largest AGC on-treatment data to date. First, although tumor genomics reciprocally shape the TME during gastric cancer tumorigenesis, we did not observe clear baseline genomic features associated with benefit from cytotoxic chemotherapy, consistent with prior work in a larger heterogeneous gastroesophageal dataset (44). Nor did we observe significant changes in mutational processes early on treatment, arguing against newly acquired tumor cell genomic changes as a major driver of early chemotherapy resistance, consistent with recent reports (45). We fully acknowledge that intrapatient heterogeneity and clonal evolution occur in all patient cohorts and tumors, particularly under the pressures of therapies, though less is known about the role in chemotherapy compared with immunotherapies (46). Gastric cancer is a particularly heterogeneous disease with high degrees of intrapatient and intratumoral heterogeneity, and larger datasets will be needed to deeply examine the impact of heterogeneity on patient outcomes. We intentionally sampled patients early on treatment to understand early changes and expect that with longer chemotherapy exposure we would observe more changes in clonal architecture. Second, the predictive ability of baseline TME features in AGC may be limited, and we observed limited baseline differences among responders and nonresponders in our cohort. However, we show the potential of integrating early on-treatment TME changes and observe conserved favorable on-treatment features including upregulation of PD-1 pathway components, antigen presentation machinery, NK-cell infiltration, and a shift from M2 to M1 polarized macrophages. In fact, our recent work in microsatellite instability–high AGC pairing pretreatment and on-treatment sampling corroborates these favorable early on-treatment compositional changes in the immune compartment (27). Interestingly, both baseline and on-treatment increases in favorable features were more pronounced in HER2$^+$ patients, suggesting both intrinsic biological differences and the immunomodulatory effects of trastuzumab (30, 47). Finally, those patients who failed to favorably remodel their TME early on therapy did not ultimately respond to first-line chemotherapy. Among these nonresponders, there were notable trends including the lack of increase of effector T-cell abundance coupled to increases in LAG3$^+$ exhausted T cells, an exodus of DCs, and an increased B-cell population. The significance of B cells in gastric cancer remains understudied, though our data, albeit limited, are aligned with the negative impact of B-cell infiltration that has been observed in some studies (48, 49). Interestingly, nearly all nonresponding patients were PD-L1 negative and failed to upregulate PD-L1 expression on treatment. The relationship between PD-L1 expression and cytotoxic chemotherapy response has not been examined in detail, but response is numerically lower (41% vs. 46%) in PD-L1–negative patients in the large (n = 1,581) phase III CheckMate-649 trial (9).

The on-treatment expansion of LAG3$^+$ T-cell populations was observed only in nonresponders. Notably, among patients with non–small cell lung cancer, LAG3 elevation in immunotherapy-naïve samples predicts for lack of benefit from immune checkpoint inhibitors, but impact on chemotherapy response is not clear (50). Although further work is needed, the anti-LAG3 antibody relatlimab in combination with PD-1 and chemotherapy is under investigation in AGC (NCT03044613, NCT04062656, and NCT02935634). Recent work in melanoma from the phase III RELATIVITY-047 trial (nivolumab with or without relatlimab) demonstrated improved progression-free survival (10 vs. 4 months) in the relatlimab arm independent of PD-L1 expression, providing some orthogonal support for this combination (51).

Prior single-cell analyses have been limited to either small heterogeneous cohorts or patients later in their disease course where the impacts of multiple prior therapies confound understanding (52–54). Importantly, none of this prior work has examined on-treatment changes which provide a unique window into the earlier effect of a therapy. In future work, we plan to couple tissue analyses to peripheral blood (circulating tumor DNA and plasma proteomics) to both annotate peripheral findings to tissue TME changes and explore more clinically accessible approaches that may serve as surrogates for serial biopsies performed in this analysis. Recent work in melanoma suggests the possibility of plasma proteomic analyses to reflect tissue-level TME features (55). Our observations lack functional validation and do not explain why, despite similar baseline TME and genomic composition, some patients fail to favorably remodel their TME, which remains a critical knowledge gap to optimally select patients for TME-directed therapeutic combinations. Functionalizing the TME is complicated, and limited model systems coupled to a general lack of standardized strategies and assessment metrics remain barriers to functional validation.

Considering our data, we are pointed toward a potential model to suggest where combination chemotherapy and PD-1–blocking agents may be most successful. When

Figure 5. Profiling the TME of nonresponders identifies an increase in LAG3$^+$ T cells. **A,** UMAP embedding T-cell subpopulations. Multiple clusters represent various subtypes of T cells in the TME of AGC. Bar plots demonstrating relative proportions of T-cell subtypes in pretreatment and posttreatment AGC samples (plot **A** inset). **B,** The bottom plot illustrates relative proportion of exhausted CD8 subpopulations in pretreatment and on-treatment samples from patients with *MET*-amplified AGC (left) and patients with AGC with wild-type *MET* (right). Top plot shows feature plots visualizing the presence of tumoral *MET* amplification (left) and the expression of *TIGIT* (right) in T-cell populations. **C,** A representative case of a patient with MET-amplified AGC (EP-07). The tumor did not radiographically respond to two cycles of XELOX in combination with pembrolizumab. Pie charts show proportion of exhausted CD8 T-cell subtypes in pretreatment and on-treatment samples. **D** and **E,** mIF images characterizing the TME of AGC before and during first-line chemotherapy in two representative nonresponders: EP-07 (**D**) and EP-08 (**E**). **F,** The expression profile of LAG3 in T-cell populations increases in nonresponders. LAG3 gene expression of T cells from scRNA-seq (top). Proportion of T cells expressing LAG3 in mIF (pie charts). LAG3 protein expression in mIF (bottom). The tumor volume of the on-treatment sample from EP-05 (annotated by asterisk) was relatively low to estimate LAG3 expression in mIF. WT, wild type; M, male; PD, progressive disease; PR, partial response.

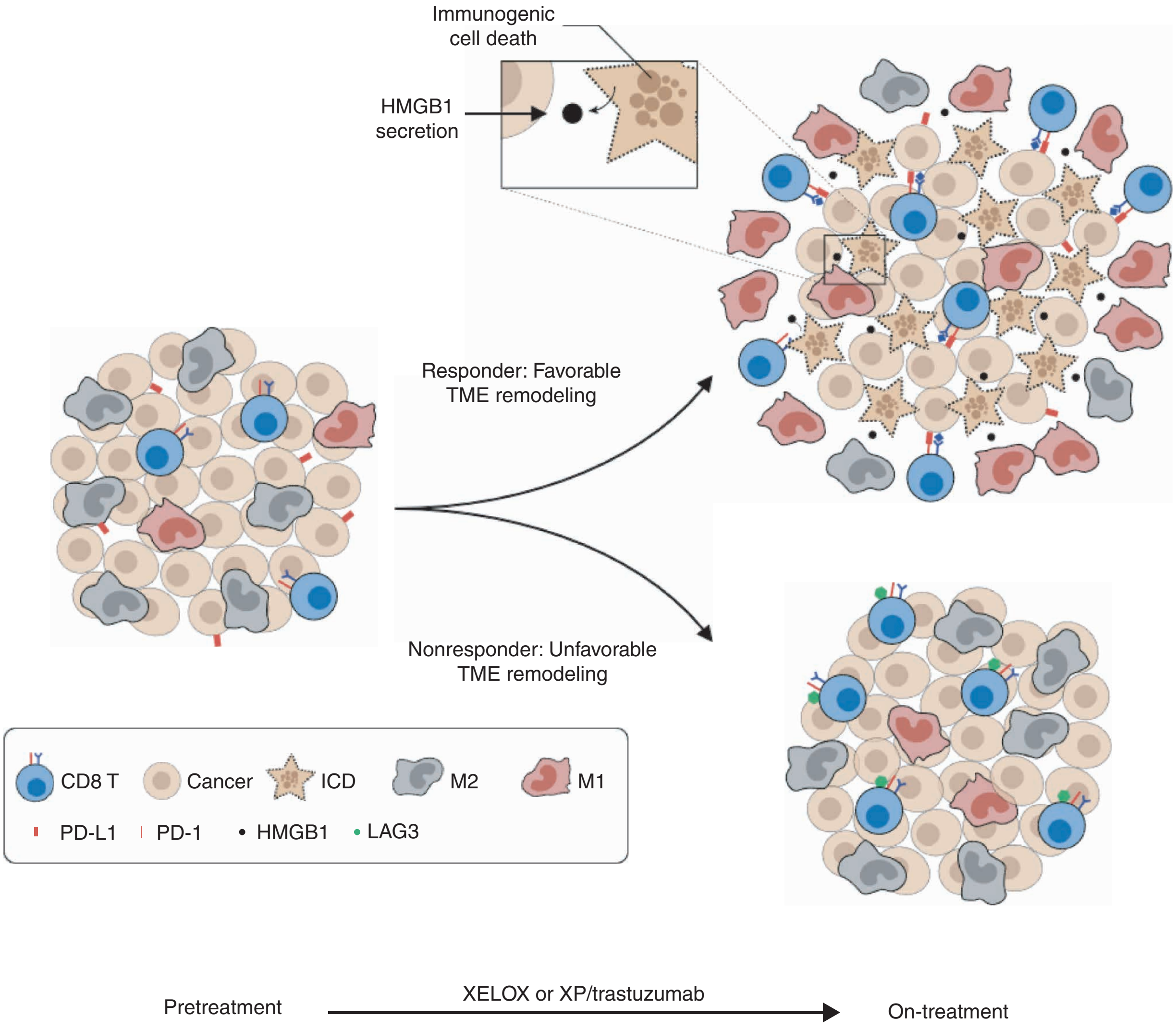

Figure 6. Putative model underlying chemotherapy response in AGC. Patients with favorable TME remodeling may be primed for synergistic interactions between immune checkpoint inhibitor and chemotherapy. Response to first-line treatment was associated with chemotherapy-induced cell death of tumor cells and on-treatment remodeling of TME, including M1-macrophage repolarization and increased effector T-cell infiltration. In contrast, inability to repolarize M2 macrophages and upregulate PD-L1 expression, coupled with infiltration of LAG3-expressing T cells, may modulate resistance to chemotherapy. ICD, immunologic cell death.

treatment-naïve gastric cancers are exposed to cytotoxic therapy, induction of innate immune components including macrophages and NK cells drives antigen presentation, on-treatment PD-L1 upregulation, and T-cell infiltration (Fig. 6). Among these patients, the additive/synergistic effects of PD-1 with chemotherapy likely further enhance response, perhaps underlying the improved clinical outcomes in PD-L1$^+$ patients. Among patients not responding to standard chemotherapy, and perhaps more commonly in PD-L1–negative tumors, chemotherapy fails to appropriately remodel the TME and immunosuppressive features (exhausted T cells, Treg persistence, B-cell increase, and persistent TAM populations) dominate. In this context, addition of anti–PD-1 agents is unlikely to provide meaningful benefit, and it is this population who are need of rational combinations beyond the addition of PD-1 alone. Detailed mechanistic studies are needed to validate this putative model and help explain why the TME in some patients does not change to favorable immune features during chemotherapy. Whether or not ongoing approaches directed at IL2, Toll-like receptors 7 and 8, CCL2/CCR2, and WNT and MDSC modulation (DKN-01) will help to recapitulate a more favorable TME seen in our data remains to be seen. Interestingly, in a small phase II trial, the addition of DKN-01 to 5-FU/oxaliplatin and PD-1 blockade appeared to enhance activity in both PD-L1–negative and particularly DKK1-high gastroesophageal adenocarcinomas perhaps reflecting modulation of unfavorable TME features (56). Ongoing studies earlier in the disease paradigm (nonmetastatic patients) when tumor–immune interactions are earlier in evolution will also be important orthogonal data. We currently have an ongoing trial designed to examine TME changes when the anti–PD-1 antibody pembrolizumab is added to standard first-line treatment with 5-FU and oxaliplatin. Patients receive serial sampling at baseline, on chemotherapy but pre-pembrolizumab, and then on the chemotherapy/immunotherapy combination (NCT# 04249739). These data are expected to further map the TME changes over the course of therapy. In fact, in the small subset of patients ($n = 17$) from this trial herein, there was similar on-treatment remodeling as seen in our primary cohort.

Overall, we provide an initial and validation dataset in treatment-naïve AGC that helps to generate a detailed TME map to contextualize novel combination approaches being tested clinically. We demonstrate that on-treatment sampling is possible and provides valuable insights into the effects of our standard therapies in AGC.

METHODS

Study Design and Participants

Eligible patients were required to meet the following criteria: (i) at least 19 years old, (ii) histologically confirmed diagnosis of unresectable, metastatic gastric cancer, (iii) adequate organ function per protocol, and (iv) Eastern Cooperative Oncology Group performance status of 0 or 1. All patients were naïve to prior chemotherapy. The trial protocol was approved by the Institutional Review Board (IRB) of Samsung Medical Center (Seoul, Korea; IRB No. 2019-11-089) and was conducted in accordance with the Declaration of Helsinki and the Guidelines for Good Clinical Practice. All patients provided written informed consent before enrollment.

At the discretion of the treating investigator, patients initially received 130 mg/m^2 of intravenous oxaliplatin infused over 120 minutes (or 80 mg/m^2 of intravenous cisplatin infused over 60–120 minutes) on day 1 and 1,000 mg/m^2 of oral capecitabine twice a day for 2 weeks followed by 1 week off. A treatment cycle consisted of 3 weeks. In addition, patients with HER-positive AGC (defined as IHC 3+ or 2+ with *HER2*:CEP17 FISH ratio ≥2.0) received intravenous trastuzumab [loading dose of 8 mg/kg (infused over 90 minutes) followed by maintenance dose of 6 mg/kg (infused over 30 minutes if the initial 90-minute infusion was well tolerated)] within 7 days of the first day of each 3-week cycle.

Sample Preparation

We obtained pretreatment primary tumor and matched peripheral blood samples at any time from 1 to 28 days before initiating treatment, and on-treatment tumor samples from primary gastric tumor after two treatment cycles. If tumor cellularity was estimated to be greater than 40% after a thorough pathologic review, tumor DNA and RNA were extracted from freshly obtained tumor tissues using a QIAamp Mini Kit (QIAGEN), according to the manufacturer's instructions. For DNA preparation, we used RNase A (cat. #19101; QIAGEN). We measured concentrations and 260/280-nm and 260/230-nm absorption ratios with an ND1000 spectrophotometer (Nanodrop Technologies, Thermo Fisher Scientific) and further quantified DNA/RNA using a Qubit fluorometer (Life Technologies).

WES and WTS

Sequencing was performed using genomic DNA (gDNA) from the tumor tissues and matched blood samples using a QIAamp DNA Blood Kit (QIAGEN). For generation of standard exome capture libraries, we used the Agilent SureSelect Target Enrichment protocol for an Illumina paired-end sequencing library together with 1 μg of inputted gDNA. In all cases, the SureSelect Human All Exon V6 probe set was used. We assessed the quantity and quality of DNA by PicoGreen and agarose gel electrophoresis. We diluted 1 μg of gDNA in EB buffer and sheared it to a target peak size of 150 to 200 bp using the Covaris LE220 focused ultrasonicator (Covaris Inc.) according to the manufacturer's recommendations. The fragmented DNA was repaired, and "A" was ligated to the 3′-end. Then, we ligated the fragments with Agilent adapters and amplified them using PCR. The prepared libraries were quantified using the TapeStation DNA ScreenTape D1000 (Agilent).

For exome capture, 250 ng of DNA library was mixed with hybridization buffer, blocking mixes, RNase block, and 5 μg of SureSelect all exon capture library, according to the standard Agilent SureSelect Target Enrichment protocol. Hybridization to the capture baits was conducted at 65°C using a heated thermal cycler lid option at 105°C for 24 hours on the PCR machine. The captured DNA was washed and amplified. The final purified product was quantified by qPCR according to the qPCR Quantification Protocol Guide (KAPA Library Quantification Kits for Illumina Sequencing platforms) and qualified using the TapeStation DNA ScreenTape D1000 (Agilent). Samples were multiplexed, and flow-cell clusters were created using the TruSeq Rapid Cluster Kit and the TruSeq Rapid SBS Kit (Illumina). Indexed libraries were submitted to an Illumina HiSeq2500 (Illumina), and paired-end (2 × 100 bp) sequencing was performed.

scRNA-seq

For single-cell preparation, tumor tissue was dissociated with the gentleMACS Dissociator and Tumor Infiltrating Lymphocyte Kit (Miltenyi Biotec) according to the manufacturer's protocol. The cells were then cryopreserved in liquid nitrogen until use. All samples showed a viability of around 90% on average after thawing. scRNA-seq libraries were generated using the Chromium Single Cell 3 Library & Gel Bead Kit v3 (10 × Genomics) following the manufacturer's instructions. Briefly, the Chromium instrument was used to separate single cells into gel bead emulsions that facilitated the addition of cell-specific barcodes to all cDNAs generated during oligo-dT–primed reverse transcription. As a result, a cell barcoding sequence and Unique Molecular Identifier were added to each cDNA molecule. Libraries were constructed and sequenced at a depth of approximately 50,000 reads per cell using the HiSeq2500 platform (Illumina).

Variant Calling and Filtering of WES

WES reads were aligned to the reference human genome GRCh37 using BWA-MEM (57) followed by preprocessing steps, including duplicate marking, indel realignment, and base recalibration using the Genome Analysis Toolkit (GATK; version 4.1.1.0; ref. 58), generating analysis-ready BAM files. To establish the highly sensitive set of somatic SNVs and short indels, we initially took the unions of variant calls from MuTect2 (59) and Strelka2 (60). Default parameters were applied, and both variant callers were run with dbSNP (version 138; ref. 61), 1000G (phase I; ref. 62), and HapMap (phase III; ref. 63) data for known polymorphic sites. We filtered out variants with minimum depth < 5 or minimum alternative alleles < 2, and annotated them using the Ensembl Variant Effect Predictor (release version 87; ref. 64) with the GRCh37 database. Allele-specific copy-number variation was estimated from WES using the FACETS (version 0.6.0; ref. 65) in default quantification mode with the given tumor and paired normal BAM files.

Mutational Signature Analyses

We estimated contributions of mutational signatures to an observed mutational spectrum in each sample (i.e., the presumed amount of exposure to corresponding mutational processes) using the deconstructSigs package (version 1.6.0) in R (66). Exome regions were defined by the Agilent SureSelect V5 target region. Only somatic mutations in exome regions were considered, and trinucleotide counts were normalized by the number of times each trinucleotide context was observed in the exome region.

Processing WTS

We annotated WTS with ENSEMBL (version 98) and aligned them to the human reference genome (GRCh38) using STAR (version 2.6.1; ref. 67). We quantified RNA expression in units of transcript per million (TPM) using RSEM (version 1.3.1; ref. 68), applying the parameters recommended by the GTEx project (https://github.com/broadinstitute/gtex-pipeline/blob/master/TOPMed_RNAseq_pipeline.md). TPM values less than 1 were considered unreliable and substituted with zero. The GSVA algorithm was used to explore the whole-transcriptome dataset (23).

scRNA-seq Data Processing

We aligned scRNA-seq reads to the GRCh38 human genome reference and quantified them using a Cellranger (version 3.1.0). The data from all samples were combined in R v.3.6.0 using the Seurat package v.3.1.4 (69). We filtered out doublets using Scrublet (70). In addition, cells with low-quality libraries (<300 genes) and high mitochondrial read proportion (>20%) were filtered out. Data from each sample were normalized, scaled, and subjected to principal component analysis, followed by a batch correction using the Harmony (26). We used UMAP algorithm to reduce the dimension for visual representation, and identified cell clusters using a shared nearest neighbor modularity optimization–based clustering algorithm. We identified various cell type clusters using “FindAllMarkers” for each cluster and annotated them based on the expression of representative markers.

IHC Analysis for PD-L1

Representative tumors from each participant were obtained from formalin-fixed, paraffin-embedded (FFPE) archival biopsy samples. The tissue was arranged in a new recipient paraffin block (tissue array block) using a trephine apparatus (SuperBioChips Laboratories). Immunohistochemical staining was performed using an automatic immunostainer (Dako) according to the manufacturer’s instructions. We used the Dako PD-L1 IHC 22C3 pharmDx Kit (Agilent Technologies) with the EnVision FLEX visualization system and counterstained with hematoxylin according to the manufacturer’s instructions. PD-L1 protein expression was determined using CPS, which is the number of PD-L1–stained cells (tumor cells, lymphocytes, and macrophages) divided by the total number of viable tumor cells and multiplied by 100. The specimen was considered to express PD-L1 if CPS was ≥1.

FFPE-CODEX Multiplexed Tissue Imaging with 19 Markers

FFPE tissue blocks were retrieved from the tissue archive at the Department of Pathology & Translational Genomics of Samsung Medical Center and Yonsei University Medical Center. Representative paraffin blocks were sectioned for staining. Square glass coverslips (Electron Microscopy Sciences) were pretreated with Vectabond (Vector Labs) according to the manufacturer’s instructions as previously described. Coverslips were washed in 100% acetone for 30 seconds and air-dried, baked at 70°C for 1 hour, and stored at room temperature. The 4-μm-thick tissue sections were mounted on Vectabond-treated coverslips and stored in a coverslip storage box (Qintay) at 4°C in a vacuum desiccator (Thermo Fisher) containing drierite desiccant (Thermo Fisher) until analysis. Staining procedures were performed according to the manufacturer’s instructions using staining solution 1 (S1), 2 (S2), 3 (S3), and 4 (S4). Conjugations of oligonucleotides were performed at a 2:1 weight/weight ratio of oligonucleotide to antibody, with at least 100 mg of antibody per reaction. All centrifugation steps were at 12,000 × *g* for 8 minutes, unless otherwise specified. Purified, carrier-free antibodies (for details on clones, reporter, and barcodes, see Supplementary Table S2) were concentrated on 50 kDa filters, and sulfhydryl groups were activated. After washing the antibody at a final concentration of 400 mmol/L, oligonucleotide was added to the antibody and incubated for 2 hours at room temperature. The conjugated antibody was washed and eluted with PBS-based antibody stabilizer (Thermo Fisher) and stored at 4°C until use. For staining with 19 antibodies, coverslips were deparaffinized after baking at 70°C for at least 1 hour, followed by immersion in fresh xylene for 30 minutes. Sections were rehydrated, and heat-induced epitope retrieval was performed. Tissues were encircled, and nonspecific binding was blocked for 1 hour at room temperature using 100 mL of blocking buffer. For each coverslip, DNA-conjugated antibodies were added to 50 mL of blocking buffer on a 50-kDa filter unit, concentrated by spinning at 12,000 × *g* for 8 minutes, and resuspended in blocking buffer to a final volume of 100 mL. Bound antibodies were then visualized using the horseradish peroxidase/liquid DAB$^+$ substrate chromogen system (Agilent) according to the manufacturer’s instructions. Sections were counterstained with hematoxylin, followed by dehydration, mounting, and imaging in brightfield mode on a BZ-X710–inverted fluorescence microscope (Keyence). Automated image acquisition and fluidics exchange were performed using an Akoya CODEX instrument and CODEX driver software (Akoya Biosciences). Figures were created using templates from Biorender (https://biorender.com), and statistical analyses were performed using GraphPad Prism5.0 (GraphPad Software).

As we failed to conjugate HER2 [PATHWAY anti-HER2/neu (4B5)], MET [CONFIRM anti-Total MET (SP44) rabbit monoclonal primary antibodies (Ventana Medical Systems)], and PD-L1 (PD-L1 IHC 22C3 pharmDx, Dako) antibodies with oligonucleotides without any reason, we performed IHC for HER2 and MET in cases with overexpression, and PD-L1 in all cases with the same tissue sections after CODEX-multiplexed tissue imaging as described previously (71, 72).

Data Availability

All raw sequencing data from the primary cohort were deposited in the European Nucleotide Archive (accession number PRJEB45598). RNA-seq data from the validation cohort are available upon request.

Authors’ Disclosures

A. Mehta reports personal fees from Third Rock Ventures, Asher Biotherapeutics, BioNTech, venBio Partners, Abata Therapeutics, and Checkmate Pharmaceuticals, and grants from Bristol Myers Squibb outside the submitted work. W.-Y. Park reports personal fees and other support from Geninus Inc. during the conduct of the study. S.J. Klempner reports personal fees from Merck, Bristol Myers Squibb, Astellas, Daiichi Sankyo, Pieris, Sanofi-Aventis, and Natera Oncology, and other support from Turning Point Therapeutics outside the submitted work. J. Lee reports grants from Stand Up To Cancer Gastric Cancer Interception Award, the Korea Health Technology R&D Project, and SKKU Excellence in Research Award Research Fund during the conduct of the study. No disclosures were reported by the other authors.

Authors’ Contributions

R. Kim: Conceptualization, data curation, formal analysis, investigation, methodology, writing–original draft, writing–review and editing. **M. An:** Conceptualization, formal analysis, investigation, methodology, writing–original draft, writing–review and editing. **H. Lee:** Conceptualization, validation, investigation, methodology, writing–original draft, writing–review and editing. **A. Mehta:** Formal analysis, methodology, writing–original draft, writing–review and editing. **Y.J. Heo:** Resources, data curation, formal analysis, methodology, writing–review and editing. **K.-M. Kim:** Formal analysis, investigation, methodology, writing–review and editing. **S.-Y. Lee:** Data curation, formal analysis, writing–review and editing. **J. Moon:** Data curation, formal analysis, methodology. **S.T. Kim:** Resources, formal analysis, investigation, writing–review and editing. **B.-H. Min:** Formal analysis, investigation, methodology, writing–review and editing. **T.J. Kim:** Resources, formal analysis, methodology, writing–review and editing. **S.Y. Rha:** Resources, formal analysis, investigation, writing–review and editing. **W.K. Kang:** Resources, formal analysis, investigation, writing–review and editing. **W.-Y. Park:** Conceptualization, formal analysis, methodology, writing–original draft, writing–review and editing. **S.J. Klempner:** Conceptualization, formal analysis, investigation, writing–original draft, writing–review and editing. **J. Lee:** Conceptualization, resources, formal analysis, supervision, investigation, methodology, writing–original draft, writing–review and editing.

Acknowledgments

This study was supported by AGA Research Foundation's AGA-Gastric Cancer Foundation Ben Feinstein Memorial Research Scholar Award in Gastric Cancer (AGA2020-13-02, to S.J. Klempner), and the Stand Up to Cancer (SU2C) Gastric Cancer Interception Research Team Grant (grant number SU2C-AACR-DT-30-20) award (to H. Lee, S.J. Klempner, and J. Lee). This research grant is administered by the American Association for Cancer Research, the Scientific Partner of SU2C. This research was also supported by the SKKU Excellence in Research Award Research Fund, Sungkyunkwan University, 2020 (to J. Lee), and a grant from the Korea Health Technology R&D Project through the Korea Health Industry Development Institute (KHIDI), and funded by the Ministry of Health & Welfare, Republic of Korea (grant number HR20C0025, to S.T. Kim and K.-M. Kim).

The costs of publication of this article were defrayed in part by the payment of page charges. This article must therefore be hereby marked *advertisement* in accordance with 18 U.S.C. Section 1734 solely to indicate this fact.

Note

Supplementary data for this article are available at Cancer Discovery Online (http://cancerdiscovery.aacrjournals.org/).

Received July 5, 2021; revised October 17, 2021; accepted December 16, 2021; published first December 21, 2021.

REFERENCES

1. Bray F, Ferlay J, Soerjomataram I, Siegel RL, Torre LA, Jemal A. Global cancer statistics 2018: GLOBOCAN estimates of incidence and mortality worldwide for 36 cancers in 185 countries. CA Cancer J Clin 2018;68:394–424.
2. Ferlay J, Soerjomataram I, Dikshit R, Eser S, Mathers C, Rebelo M, et al. Cancer incidence and mortality worldwide: Sources, methods and major patterns in GLOBOCAN 2012. Int J Cancer 2015;136:E359–86.
3. Bang YJ, Van Cutsem E, Feyereislova A, Chung HC, Shen L, Sawaki A, et al. Trastuzumab in combination with chemotherapy versus chemotherapy alone for treatment of HER2-positive advanced gastric or gastro-oesophageal junction cancer (ToGA): A phase 3, open-label, randomised controlled trial. Lancet 2010;376:687–97.
4. Cunningham D, Starling N, Rao S, Iveson T, Nicolson M, Coxon F, et al. Capecitabine and oxaliplatin for advanced esophagogastric cancer. N Engl J Med 2008;358:36–46.
5. Koizumi W, Narahara H, Hara T, Takagane A, Akiya T, Takagi M, et al. S-1 plus cisplatin versus S-1 alone for first-line treatment of advanced gastric cancer (SPIRITS trial): A phase III trial. Lancet Oncol 2008;9:215–21.
6. Wilke H, Muro K, Van Cutsem E, Oh SC, Bodoky G, Shimada Y, et al. Ramucirumab plus paclitaxel versus placebo plus paclitaxel in patients with previously treated advanced gastric or gastro-oesophageal junction adenocarcinoma (RAINBOW): A double-blind, randomised phase 3 trial. Lancet Oncol 2014;15:1224–35.
7. Boku N, Ryu MH, Kato K, Chung HC, Minashi K, Lee KW, et al. Safety and efficacy of nivolumab in combination with S-1/capecitabine plus oxaliplatin in patients with previously untreated, unresectable, advanced, or recurrent gastric/gastroesophageal junction cancer: Interim results of a randomized, phase II trial (ATTRACTION-4). Ann Oncol 2019;30:250–8.
8. Fuchs CS, Doi T, Jang RW, Muro K, Satoh T, Machado M, et al. Safety and efficacy of pembrolizumab monotherapy in patients with previously treated advanced gastric and gastroesophageal junction cancer: Phase 2 clinical KEYNOTE-059 trial. JAMA Oncol 2018;4:e180013.
9. Janjigian YY, Shitara K, Moehler M, Garrido M, Salman P, Shen L, et al. First-line nivolumab plus chemotherapy versus chemotherapy alone for advanced gastric, gastro-oesophageal junction, and oesophageal adenocarcinoma (CheckMate 649): A randomised, open-label, phase 3 trial. Lancet 2021;398:27–40.
10. Kang YK, Boku N, Satoh T, Ryu MH, Chao Y, Kato K, et al. Nivolumab in patients with advanced gastric or gastro-oesophageal junction cancer refractory to, or intolerant of, at least two previous chemotherapy regimens (ONO-4538–12, ATTRACTION-2): A randomised, double-blind, placebo-controlled, phase 3 trial. Lancet 2017;390:2461–71.
11. Kato K, Shah MA, Enzinger P, Bennouna J, Shen L, Adenis A, et al. KEYNOTE-590: Phase III study of first-line chemotherapy with or without pembrolizumab for advanced esophageal cancer. Future Oncol 2019;15:1057–66.
12. Chung HC, Bang Y-J, Fuchs CS, Qin S, Satoh T, Shitara K, et al. KEYNOTE-811 pembrolizumab plus trastuzumab and chemotherapy for HER2+ metastatic gastric or gastroesophageal junction cancer (mG/GEJc): A double-blind, randomized, placebo-controlled phase III study. J Clin Oncol 2020;38:TPS463.
13. Mansoor W, Kulkarni AS, Kato K, Sun J-M, Shah MA, Enzinger PC, et al. Health-related quality of life (HRQoL) of pembrolizumab plus chemotherapy versus chemotherapy as first-line therapy in patients with advanced esophageal cancer: The phase III KEYNOTE-590 study. J Clin Oncol 2021;39:168.
14. Heinhuis KM, Ros W, Kok M, Steeghs N, Beijnen JH, Schellens JHM. Enhancing antitumor response by combining immune checkpoint inhibitors with chemotherapy in solid tumors. Ann Oncol 2019;30:219–35.
15. Park DS, Robertson-Tessi M, Luddy KA, Maini PK, Bonsall MB, Gatenby RA, et al. The goldilocks window of personalized chemotherapy: Getting the immune response just right. Cancer Res 2019;79:5302–15.
16. Tel J, Hato SV, Torensma R, Buschow SI, Figdor CG, Lesterhuis WJ, et al. The chemotherapeutic drug oxaliplatin differentially affects blood DC function dependent on environmental cues. Cancer Immunol Immunother 2012;61:1101–11.
17. Wang W, Wu L, Zhang J, Wu H, Han E, Guo Q. Chemoimmunotherapy by combining oxaliplatin with immune checkpoint blockades reduced tumor burden in colorectal cancer animal model. Biochem Biophys Res Commun 2017;487:1–7.
18. Galetto A, Buttiglieri S, Forno S, Moro F, Mussa A, Matera L. Drug- and cell-mediated antitumor cytotoxicities modulate cross-presentation of tumor antigens by myeloid dendritic cells. Anticancer Drugs 2003;14:833–43.
19. Vincent J, Mignot G, Chalmin F, Ladoire S, Bruchard M, Chevriaux A, et al. 5-Fluorouracil selectively kills tumor-associated myeloid-derived suppressor cells resulting in enhanced T cell-dependent antitumor immunity. Cancer Res 2010;70:3052–61.
20. Cancer Genome Atlas Research Network. Comprehensive molecular characterization of gastric adenocarcinoma. Nature 2014;513:202–9.
21. Alexandrov LB, Kim J, Haradhvala NJ, Huang MN, Tian Ng AW, Wu Y, et al. The repertoire of mutational signatures in human cancer. Nature 2020;578:94–101.
22. Bagaev A, Kotlov N, Nomie K, Svekolkin V, Gafurov A, Isaeva O, et al. Conserved pan-cancer microenvironment subtypes predict response to immunotherapy. Cancer Cell 2021;39:845–65.

23. Hanzelmann S, Castelo R, Guinney J. GSVA: Gene set variation analysis for microarray and RNA-seq data. BMC Bioinf 2013;14:7.
24. Coates PJ, Rundle JK, Lorimore SA, Wright EG. Indirect macrophage responses to ionizing radiation: Implications for genotype-dependent bystander signaling. Cancer Res 2008;68:450–6.
25. Parsons MJ, Tammela T, Dow LE. WNT as a driver and dependency in cancer. Cancer Discov 2021;11:2413–29.
26. Korsunsky I, Millard N, Fan J, Slowikowski K, Zhang F, Wei K, et al. Fast, sensitive and accurate integration of single-cell data with Harmony. Nat Methods 2019;16:1289–96.
27. Kwon M, An M, Klempner SJ, Lee H, Kim KM, Sa JK, et al. Determinants of response and intrinsic resistance to PD-1 blockade in microsatellite instability-high gastric cancer. Cancer Discov 2021;11:2168–85.
28. Galluzzi L, Buque A, Kepp O, Zitvogel L, Kroemer G. Immunogenic cell death in cancer and infectious disease. Nat Rev Immunol 2017;17:97–111.
29. Wang Z, Chen J, Hu J, Zhang H, Xu F, He W, et al. cGAS/STING axis mediates a topoisomerase II inhibitor-induced tumor immunogenicity. J Clin Invest 2019;129:4850–62.
30. Wu S, Zhang Q, Zhang F, Meng F, Liu S, Zhou R, et al. HER2 recruits AKT1 to disrupt STING signalling and suppress antiviral defence and antitumour immunity. Nat Cell Biol 2019;21:1027–40.
31. Jayasingam SD, Citartan M, Thang TH, Mat Zin AA, Ang KC, Ch'ng ES. Evaluating the polarization of tumor-associated macrophages into M1 and M2 phenotypes in human cancer tissue: Technicalities and challenges in routine clinical practice. Front Oncol 2019;9:1512.
32. Langlais D, Barreiro LB, Gros P. The macrophage IRF8/IRF1 regulome is required for protection against infections and is associated with chronic inflammation. J Exp Med 2016;213:585–603.
33. Vogl T, Eisenblatter M, Voller T, Zenker S, Hermann S, van Lent P, et al. Alarmin S100A8/S100A9 as a biomarker for molecular imaging of local inflammatory activity. Nat Commun 2014;5:4593.
34. Chen Q, Han B, Meng X, Duan C, Yang C, Wu Z, et al. Immunogenomic analysis reveals LGALS1 contributes to the immune heterogeneity and immunosuppression in glioma. Int J Cancer 2019;145:517–30.
35. Lee HO, Hong Y, Etlioglu HE, Cho YB, Pomella V, Van den Bosch B, et al. Lineage-dependent gene expression programs influence the immune landscape of colorectal cancer. Nat Genet 2020;52:594–603.
36. Wilson JL, Mayr HK, Weichhart T. Metabolic programming of macrophages: Implications in the pathogenesis of granulomatous disease. Front Immunol 2019;10:2265.
37. Street K, Risso D, Fletcher RB, Das D, Ngai J, Yosef N, et al. Slingshot: Cell lineage and pseudotime inference for single-cell transcriptomics. BMC Genomics 2018;19:477.
38. Newman AM, Steen CB, Liu CL, Gentles AJ, Chaudhuri AA, Scherer F, et al. Determining cell type abundance and expression from bulk tissues with digital cytometry. Nat Biotechnol 2019;37:773–82.
39. Steen CB, Liu CL, Alizadeh AA, Newman AM. Profiling cell type abundance and expression in bulk tissues with CIBERSORTx. Methods Mol Biol 2020;2117:135–57.
40. Janjigian YY, Maron SB, Chatila WK, Millang B, Chavan SS, Alterman C, et al. First-line pembrolizumab and trastuzumab in HER2-positive oesophageal, gastric, or gastro-oesophageal junction cancer: An open-label, single-arm, phase 2 trial. Lancet Oncol 2020;21:821–31.
41. Beltra JC, Manne S, Abdel-Hakeem MS, Kurachi M, Giles JR, Chen Z, et al. Developmental relationships of four exhausted CD8(+) T cell subsets reveals underlying transcriptional and epigenetic landscape control mechanisms. Immunity 2020;52:825–41.
42. Bejarano L, Jordao MJC, Joyce JA. Therapeutic targeting of the tumor microenvironment. Cancer Discov 2021;11:933–59.
43. Derks S, de Klerk LK, Xu X, Fleitas T, Liu KX, Liu Y, et al. Characterizing diversity in the tumor-immune microenvironment of distinct subclasses of gastroesophageal adenocarcinomas. Ann Oncol 2020;31:1011–20.
44. Janjigian YY, Sanchez-Vega F, Jonsson P, Chatila WK, Hechtman JF, Ku GY, et al. Genetic predictors of response to systemic therapy in esophagogastric cancer. Cancer Discov 2018;8:49–58.
45. van de Haar J, Hoes LR, Roepman P, Lolkema MP, Verheul HMW, Gelderblom H, et al. Limited evolution of the actionable metastatic cancer genome under therapeutic pressure. Nat Med 2021;27:1553–63.
46. Vitale I, Shema E, Loi S, Galluzzi L. Intratumoral heterogeneity in cancer progression and response to immunotherapy. Nat Med 2021;27:212–24.
47. Candas-Green D, Xie B, Huang J, Fan M, Wang A, Menaa C, et al. Dual blockade of CD47 and HER2 eliminates radioresistant breast cancer cells. Nat Commun 2020;11:4591.
48. Fristedt R, Borg D, Hedner C, Berntsson J, Nodin B, Eberhard J, et al. Prognostic impact of tumour-associated B cells and plasma cells in oesophageal and gastric adenocarcinoma. J Gastrointest Oncol 2016;7:848–59.
49. Hennequin A, Derangere V, Boidot R, Apetoh L, Vincent J, Orry D, et al. Tumor infiltration by Tbet+ effector T cells and CD20+ B cells is associated with survival in gastric cancer patients. Oncoimmunology 2016;5:e1054598.
50. Datar I, Sanmamed MF, Wang J, Henick BS, Choi J, Badri T, et al. Expression analysis and significance of PD-1, LAG-3, and TIM-3 in human non-small cell lung cancer using spatially resolved and multiparametric single-cell analysis. Clin Cancer Res 2019;25:4663–73.
51. Lipson EJ, Tawbi HA-H, Schadendorf D, Ascierto PA, Matamala L, Gutiérrez EC, et al. Relatlimab (RELA) plus nivolumab (NIVO) versus NIVO in first-line advanced melanoma: Primary phase III results from RELATIVITY-047 (CA224–047). J Clin Oncol 2021;39:9503.
52. Sathe A, Grimes SM, Lau BT, Chen J, Suarez C, Huang RJ, et al. Single-cell genomic characterization reveals the cellular reprogramming of the gastric tumor microenvironment. Clin Cancer Res 2020;26:2640–53.
53. Wang R, Dang M, Harada K, Han G, Wang F, Pool Pizzi M, et al. Single-cell dissection of intratumoral heterogeneity and lineage diversity in metastatic gastric adenocarcinoma. Nat Med 2021;27:141–51.
54. Zhang M, Hu S, Min M, Ni Y, Lu Z, Sun X, et al. Dissecting transcriptional heterogeneity in primary gastric adenocarcinoma by single cell RNA sequencing. Gut 2021;70:464–75.
55. Chen R, Smith EC, Chan SWS, Hueniken K, Brown MC, Majeed H, et al. Comparison of care patterns for hospitalized immune-related adverse events (irAEs) between melanoma patients on combination immune checkpoint inhibitor (ICI) therapy versus ICI monotherapy. J Clin Oncol 2019;37:85.
56. Klempner SJ, Chao J, Chiu V, Mahalingam D, Uronis H, Kagey M, et al. DKN-01 in combination with tislelizumab and chemotherapy as a first-line therapy in unselected patients with advanced gastroesophageal adenocarcinoma (GEA): DisTinGuish trial. Ann Oncol 2021;32:S1040–75.
57. Li H, Durbin R. Fast and accurate short read alignment with Burrows-Wheeler transform. Bioinformatics 2009;25:1754–60.
58. McKenna A, Hanna M, Banks E, Sivachenko A, Cibulskis K, Kernytsky A, et al. The Genome Analysis Toolkit: A MapReduce framework for analyzing next-generation DNA sequencing data. Genome Res 2010;20:1297–303.
59. Cibulskis K, Lawrence MS, Carter SL, Sivachenko A, Jaffe D, Sougnez C, et al. Sensitive detection of somatic point mutations in impure and heterogeneous cancer samples. Nat Biotechnol 2013;31:213–9.
60. Kim S, Scheffler K, Halpern AL, Bekritsky MA, Noh E, Kallberg M, et al. Strelka2: Fast and accurate calling of germline and somatic variants. Nat Methods 2018;15:591–4.
61. Sherry ST, Ward MH, Kholodov M, Baker J, Phan L, Smigielski EM, et al. dbSNP: The NCBI database of genetic variation. Nucleic Acids Res 2001;29:308–11.
62. Genomes Project Consortium, Auton A, Brooks LD, Durbin RM, Garrison EP, Kang HM, et al. A global reference for human genetic variation. Nature 2015;526:68–74.
63. International HapMap Consortium, Altshuler DM, Gibbs RA, Peltonen L, Altshuler DM, Gibbs RA, et al. Integrating common and rare genetic variation in diverse human populations. Nature 2010;467:52–8.
64. McLaren W, Gil L, Hunt SE, Riat HS, Ritchie GR, Thormann A, et al. The ensembl variant effect predictor. Genome Biol 2016;17:122.

65. Shen R, Seshan VE. FACETS: Allele-specific copy number and clonal heterogeneity analysis tool for high-throughput DNA sequencing. Nucleic Acids Res 2016;44:e131.
66. Rosenthal R, McGranahan N, Herrero J, Taylor BS, Swanton C. DeconstructSigs: Delineating mutational processes in single tumors distinguishes DNA repair deficiencies and patterns of carcinoma evolution. Genome Biol 2016;17:31.
67. Dobin A, Davis CA, Schlesinger F, Drenkow J, Zaleski C, Jha S, et al. STAR: Ultrafast universal RNA-seq aligner. Bioinformatics 2013;29:15–21.
68. Li B, Dewey CN. RSEM: Accurate transcript quantification from RNA-Seq data with or without a reference genome. BMC Bioinf 2011;12:323.
69. Stuart T, Butler A, Hoffman P, Hafemeister C, Papalexi E, Mauck WM 3rd, et al. Comprehensive integration of single-cell data. Cell 2019;177:1888–902.
70. Wolock SL, Lopez R, Klein AM. Scrublet: Computational Identification of cell doublets in single-cell transcriptomic data. Cell Syst 2019;8:281–91.
71. Schurch CM, Bhate SS, Barlow GL, Phillips DJ, Noti L, Zlobec I, et al. Coordinated cellular neighborhoods orchestrate antitumoral immunity at the colorectal cancer invasive front. Cell 2020;182:1341–59.
72. Goltsev Y, Samusik N, Kennedy-Darling J, Bhate S, Hale M, Vazquez G, et al. Deep profiling of mouse splenic architecture with CODEX multiplexed imaging. Cell 2018;174:968–81.